




Coordinated demethylation of H3K9 and H3K27 is required for rapid inflammatory responses of endothelial cells

Yoshiki Higashijima^{1,2}, Yusuke Matsui³, Teppei Shimamura⁴, Ryo Nakaki⁵, Nao Nagai⁶, Shuichi Tsutsumi⁷, Yohei Abe⁸, Verena M Link^{8,9,10}, Mizuko Osaka^{11,12}, Masayuki Yoshida¹², Ryo Watanabe¹³, Toshihiro Tanaka^{13,14}, Akashi Taguchi², Mai Miura^{2,15}, Xiaoan Ruan¹⁶, Guoliang Li¹⁷ , Tsuyoshi Inoue¹⁸ , Masaomi Nangaku¹⁸, Hiroshi Kimura¹⁹, Tetsushi Furukawa¹, Hiroyuki Aburatani⁷, Youichiro Wada², Yijun Ruan¹⁶, Christopher K Glass^{8,20,*} & Yasuharu Kanki^{2,**} 

Abstract

Histone H3 lysine-9 di-methylation (H3K9me2) and lysine-27 trimethylation (H3K27me3) are linked to repression of gene expression, but the functions of repressive histone methylation dynamics during inflammatory responses remain enigmatic. Here, we report that lysine demethylases 7A (KDM7A) and 6A (UTX) play crucial roles in tumor necrosis factor (TNF)- α signaling in endothelial cells (ECs), where they are regulated by a novel TNF- α -responsive microRNA, miR-3679-5p. TNF- α rapidly induces co-occupancy of KDM7A and UTX at nuclear factor kappa-B (NF- κ B)-associated elements in human ECs. KDM7A and UTX demethylate H3K9me2 and H3K27me3, respectively, and are both required for activation of NF- κ B-dependent inflammatory genes. Chromosome conformation capture-based methods furthermore uncover increased interactions between TNF- α -induced super enhancers at NF- κ B-relevant loci, coinciding with KDM7A and UTX recruitments. Simultaneous pharmacological inhibition of KDM7A and UTX significantly reduces

leukocyte adhesion in mice, establishing the biological and potential translational relevance of this mechanism. Collectively, these findings suggest that rapid erasure of repressive histone marks by KDM7A and UTX is essential for NF- κ B-dependent regulation of genes that control inflammatory responses of ECs.

Keywords chromatin conformation; endothelial dysfunction; histone demethylase; repressive histone mark; super enhancer

Subject Categories Chromatin, Transcription & Genomics; Immunology

DOI 10.15252/emboj.2019103949 | Received 10 November 2019 | Revised 27 January 2020 | Accepted 4 February 2020 | Published online 3 March 2020

The EMBO Journal (2020) 39: e103949

Introduction

Precise control of inflammation is essential for the immune system and the maintenance of tissue homeostasis in higher eukaryotes.

- 1 Department of Bioinformational Pharmacology, Tokyo Medical and Dental University, Tokyo, Japan
- 2 Isotope Science Center, The University of Tokyo, Tokyo, Japan
- 3 Division of Biomedical and Health Informatics, Graduate school of medicine, Nagoya university, Nagoya, Japan
- 4 Division of Systems Biology, Nagoya University Graduate School of Medicine, Nagoya, Japan
- 5 Rhelixa Inc., Tokyo, Japan
- 6 Department of Microbiology and Immunology, Keio University School of Medicine, Tokyo, Japan
- 7 Division of Genome Sciences, RCAST, The University of Tokyo, Tokyo, Japan
- 8 Department of Cellular and Molecular Medicine, School of Medicine, University of California, San Diego, La Jolla, CA, USA
- 9 Faculty of Biology, Division of Evolutionary Biology, Ludwig-Maximilian University of Munich, Munich, Germany
- 10 Metaorganism Immunity Section, Laboratory of Immune System Biology, National Institute of Allergy and Infectious Diseases, National Institutes of Health, Bethesda, MD, USA
- 11 Department of Nutrition in Cardiovascular Disease, Tokyo Medical and Dental University, Tokyo, Japan
- 12 Department of Life Sciences and Bioethics, Tokyo Medical and Dental University, Tokyo, Japan
- 13 Department of Human Genetics and Disease Diversity, Graduate School of Medical and Dental Sciences, Tokyo Medical and Dental University, Tokyo, Japan
- 14 Bioresource Research Center, Tokyo Medical and Dental University, Tokyo, Japan
- 15 Laboratory for Systems Biology and Medicine, RCAST, The University of Tokyo, Tokyo, Japan
- 16 Jackson Laboratory for Genomic Medicine, Farmington, CT, USA
- 17 Agricultural Bioinformatics Key Laboratory of Hubei Province, Hubei Engineering Technology Research Center of Agricultural Big Data, College of Informatics, Huazhong Agricultural University, Wuhan, China
- 18 Division of Nephrology and Endocrinology, The University of Tokyo Graduate School of Medicine, Tokyo, Japan
- 19 Cell Biology Center, Institute of Innovative Research, Tokyo Institute of Technology, Yokohama, Japan
- 20 Department of Medicine, University of California, San Diego, La Jolla, CA, USA

*Corresponding author. Tel: +1 (858) 534 6011; E-mail: ckg@ucsd.edu

**Corresponding author. Tel: +81 3 5841 3055; E-mail: kanki@lsbm.org

Insufficient inflammatory responses increase the risk of contracting infectious diseases, while excessive or inadequate responses contribute to many common and life-threatening illnesses. Atherosclerosis is an example of a chronic low-grade inflammatory disease of arteries, mediated by the accumulation of plaque within the blood vessel walls. Heart attack and stroke as a sequel of atherosclerosis are responsible for an immense burden of morbidity and mortality (Benjamin *et al*, 2017). Endothelial cells (ECs) are not only static cells that are components of the blood vessel system, but also play pivotal roles in the development of atherosclerosis. Proinflammatory stimuli, such as hemodynamic turbulence, hyperlipidemia, and inflammatory cytokines, induce the expression of adhesion molecules on the luminal EC surface, which causes leukocyte recruitment and a subsequent cascade of inflammatory processes (Libby, 2002; Libby *et al*, 2011; Gistera & Hansson, 2017). Although the aberrant expression of adhesion molecules has been implicated in the initiation step of atherosclerosis, the molecular mechanisms responsible for the induction of adhesion molecules are currently incompletely understood.

Recent technological advances in next-generation sequencing (NGS) have revealed that epigenetic modifications, including DNA methylation, histone modification, non-coding RNA, and chromosomal conformation, influence gene expression, thus contributing to the regulation of cell fate, the maintenance of cell specificity, and cell type-specific functions (Roadmap Epigenomics *et al*, 2015). In vascular development, histone modifications correlate with master transcription factors during EC differentiation from embryonic stem (ES) cells (Kanki *et al*, 2017). In addition, to maintain EC specificity, the transcription factor GATA2 regulates EC-specific gene expression, correlated with the cell type-specific chromatin conformation and histone modifications (Kanki *et al*, 2011). In ECs, several miRNAs reportedly regulate the balance of pro- or anti-inflammatory signaling pathways in response to external stimuli, including oscillatory flow and inflammatory cytokines (Feinberg & Moore, 2016). Consistently, we previously reported that tumor necrosis factor (TNF)- α -responsive miRNAs not only co-associate with TNF- α -responsive coding genes but also with genes harboring miRNAs, suggesting that transcriptional factories specialized to produce non-coding transcripts control the inflammatory responses (Papantonis *et al*, 2012). Our group has also reported that interleukin-4 induced adhesion molecules, through transcription factor STAT6-mediated histone modification changes, in cultured human ECs (Tozawa *et al*, 2011). Taken together, epigenetic regulations in ECs play critical roles in the initiation and progression of vascular-related diseases, including atherosclerosis.

The post-transcriptional modifications (methylation, acetylation, and ubiquitination) of histone tails correlate with the chromatin state of either activated or repressed transcription of the associated genes. In particular, di-methylation of histone H3 at lysine 9 (H3K9me2) and tri-methylation of histone H3 at lysine 27 (H3K27me3) are mostly associated with gene repression. Several *in vitro* differentiation studies have demonstrated that the jumonji C (JmjC) domain-containing protein, ubiquitously transcribed tetratricopeptide repeat, X linked (UTX), also known as KDM6A, demethylates H3K27me3 and is required for the activation of specific gene expression during lineage commitment (Agger *et al*, 2007; Lan *et al*, 2007). Previous studies have also demonstrated UTX-mediated demethylation of H3K27me3 at tissue-specific enhancer was critical to activate cardiac

developmental and myogenic programs (Seenundun *et al*, 2010; Lee *et al*, 2012; Faralli *et al*, 2016). In addition, exome- and genome-wide sequencing strategies have identified UTX mutations and deletions in multiple cancer types, including leukemia (van Haaften *et al*, 2009; Dalglish *et al*, 2010; Gui *et al*, 2011; Cancer Genome Atlas Research *et al*, 2013; Huether *et al*, 2014; Ntziachristos *et al*, 2014; Bailey *et al*, 2016), indicating the possible role of UTX as a tumor suppressor in cancer biology. Another JmjC domain-containing protein, lysine demethylase 7A (KDM7A), also known as JHDM1D, contains a plant homeo domain (PHD) and demethylates H3K9me2 and H3K27me2. KDM7A functions as an eraser of silencing marks on chromatin, mostly during brain development, cell differentiation, cell cycle, and cell proliferation (Horton *et al*, 2010; Tsukada *et al*, 2010; Osawa *et al*, 2011). Although the significance of histone demethylases in transcriptional control during development and in cancer has been extensively studied, fewer studies have examined the potential roles of histone demethylases in acute responses, including inflammation in terminally differentiated cells (De Santa *et al*, 2007, 2009; Kruidenier *et al*, 2012).

Inflammatory responses are controlled by master transcription factors, including Nuclear factor kappa-B (NF- κ B) (Zhang *et al*, 2017). NF- κ B cooperatively interacts at *cis*-regulatory elements (*i.e.*, proximal promoters and distal enhancers) in a context-dependent manner to elicit the appropriate gene expression profiles. NF- κ B binding is coupled with the dynamic remodeling of the epigenetic landscape and chromatin structure, to change global gene expression patterns responsible for cell fate, phenotype, and behavior. Previous studies of transcription factor binding profiles in different cell types and conditions revealed that most binding occurs in intronic or intergenic regions, showing that enhancers play crucial roles in determining the cell type-specific transcriptome (Adam *et al*, 2015; Heinz *et al*, 2015; Saint-Andre *et al*, 2016). Other studies demonstrated the importance of super enhancers (SEs), also known as stretch or large enhancer clusters, for the regulation of genes correlated with cell identity (Hnisz *et al*, 2013; Parker *et al*, 2013; Whyte *et al*, 2013; Suzuki *et al*, 2017). The expression of genes associated with SEs is particularly sensitive to outside stimuli, including inflammatory cytokines, which may control and facilitate cell state transitions (Brown *et al*, 2014b; Hah *et al*, 2015; Schmidt *et al*, 2015). In human ECs, TNF- α -induced SEs display extremely high occupancies of NF- κ B, active histone marks (H3K27ac), and the epigenetic reader protein bromodomain-containing protein 4 (BRD4). The pharmacological inhibition of BRD4 by JQ1 inhibited a broad range of TNF- α -responsive genes, suggesting the important role of SEs in the inflammatory response of ECs (Brown *et al*, 2014b). More recently, Beyaz *et al* showed that UTX facilitates the accessibility of SEs that establish the cell identity of invariant natural killer T cells, in accordance with low levels of H3K27me3 (Beyaz *et al*, 2017). This study raised the possibility that the erasure of repressive histone marks by histone demethylases correlates with the formation of SEs and the activation of associated genes; however, these points have not been addressed during the early inflammatory responses.

Recent advances in chromosome conformation capture (3C)-based technologies have emphasized the relevance of the three-dimensional (3D) genome organization for transcriptional control. Chromatin interaction analysis with paired-end tag sequencing (ChIA-PET) (Fullwood *et al*, 2009) and HiChIP (Mumbach *et al*,

2016) has identified chromatin loops (*e.g.*, promoter–enhancer interactions) mediated by specific protein factors, which are functionally associated with gene expression programs. Hi-C (Lieberman-Aiden *et al*, 2009) has also revealed that the genome is organized into topologically associating domains (TADs) of several hundred kilobases to a few megabases, which play important roles in genome organization and proper control of gene expression. Megabase TADs are reportedly already formed in ES cells and largely conserved through development, among different cell types and in response to specific stimuli (Dixon *et al*, 2012; Jin *et al*, 2013), although recent studies have suggested that submegabase (sub)-TADs could have plastic properties (Phillips-Cremins *et al*, 2013; Siersbaek *et al*, 2017; Kim *et al*, 2018; Ogiyama *et al*, 2018). Furthermore, using 3C, circular 3C (4C), and ChIA-PET, we showed that human ECs have cell type-specific small chromatin loops, which correlate with gene expression profiles (Kanki *et al*, 2011; Mimura *et al*, 2012; Papanonis *et al*, 2012; Inoue *et al*, 2014). However, there is no clear consensus on the plasticity of chromatin interactions (*i.e.*, chromatin loops or small TADs) in response to external stimuli, particularly in terminally differentiated cells.

In this study, we identified a novel TNF- α -responsive miRNA, miR-3679-5p, which inhibits the induction of adhesion molecules by targeting two histone demethylases, KDM7A and UTX, in cultured human ECs. Importantly, an RNA-seq analysis revealed that KDM7A and UTX cooperatively control the expression of not only adhesion molecules but also many other NF- κ B-dependent genes. Consistent with this, TNF- α stimuli recruited KDM7A and UTX to the NF- κ B-related elements, where the repressive histone marks H3K9me2 and H3K27me3 were rapidly removed. Furthermore, Hi-C in combination with ChIA-PET revealed that TNF- α -responsive SE-SE interactions were newly formed within sub-TADs, immediately following TNF- α stimulation. Finally, the pharmacological inhibition of KDM7A and UTX led to the reduction of leukocyte adhesive interactions on the surfaces of TNF- α -activated ECs in mice. Taken together, these data suggest that erasing repressive histone marks by histone demethylases within NF- κ B-related regions could be a cue during inflammatory responses in ECs. Our findings about the cooperative functions of these two histone demethylases give new insights into the initiation of atherosclerosis and may provide therapeutic opportunities for the treatments of vascular inflammatory diseases.

Results

A novel miRNA, miR-3679-5p, inhibits monocyte adhesion to ECs

To explore the transcriptional regulatory dynamics that occur during the inflammatory activation of ECs, we activated human umbilical vein ECs with 10 ng/ml of TNF- α , a canonical proinflammatory stimulus, for 4 and 24 h and analyzed the whole transcriptome by NGS. As a result, the TNF- α -up-regulated genes (656; more than 2-fold by TNF- α treatment) can be divided into two classes, those that are strongly induced at 4 h (class 1) and those that are strongly induced at 24 h (class 2). Consistent with our previous report (Tozawa *et al*, 2011), important adhesion molecules involved in monocyte recruitment to atherosclerotic lesions, including vascular cell adhesion molecule 1 (VCAM1), intracellular adhesion molecule 1 (ICAM1), and E-selectin (SELE), were classified into class 1

(Fig 1A, Appendix Fig S1A–D). A gene ontology (GO) analysis further revealed that the class 1 and class 2 genes were commonly related to inflammatory responses, whereas the biological processes of extracellular matrix regulation were highly enriched in class 2 (Fig EV1A and B). Interestingly, TNF- α -down-regulated genes (501; < 0.5-fold by TNF- α treatment) were associated with developmental pathways, including angiogenesis and blood vessel morphogenesis (Fig EV1C and D). These data led us to speculate that during the rapid activation of terminally differentiated ECs, the inflammatory stimulation up-regulated the transcription of genes necessary for the cytokine response and repressed the genes important for the development of ECs, possibly because of the limitations of ATP and active RNA polymerase II (RNAP).

In our previous study, we noticed that the downregulation of miRNAs is coupled with the upregulation of their corresponding mRNAs and vice versa after inflammatory stimuli (Papanonis *et al*, 2012). Therefore, we hypothesized that the miRNAs intermediate rapid response of adhesion molecule induction, and performed miRNA microarray analyses of ECs at baseline and treated with TNF- α for 4 and 24 h. Probes with low expression values (raw signal < 0.1 in all conditions) were removed, and 199 miRNAs were identified in total. Based on the hypothesis that the expression levels of miRNAs that regulate adhesion molecules in class 1 of Fig 1A change after 4 h of TNF- α treatment, we selected TNF- α -responsive miRNAs (> 2-fold expression change at 4 h relative to control). Interestingly, many miRNAs were down-regulated in response to TNF- α treatment (Fig 1B) although TNF- α increased some miRNAs, including miR-155 and miR-31, which were previously reported to be up-regulated by TNF- α treatment (Suarez *et al*, 2010; Papanonis *et al*, 2012). Of 31 TNF- α -down-regulated miRNAs at 4 h, 18 miRNAs were unchanged at 24 h with or without TNF- α treatment (Fig 1B). Among them, 6 miRNAs are expressed in human ECs according to the FANTOM5 database, a collaborative omics data integration and interactive visualization system (de Rie *et al*, 2017). We further selected the top three most down-regulated miRNAs (miR-3679-5p, miR-374b-5p, miR374a-5p) and examined the effects of these miRNAs on the TNF- α -induced mRNA expression of adhesion molecules. Treatment of the cells with miR-3679-5p only significantly decreased TNF- α -induced mRNA expression of VCAM1 (Fig 1C and Appendix Fig S2A and B). Interestingly, miR-3679-5p is human-specific and not conserved in mammals, and overexpression of miR-3679-5p reduced not only the mRNA induction of VCAM1, but also those of ICAM1 and SELE (Fig 1C and D). Moreover, to test whether the reduction of these three adhesion molecules by miR-3679-5p overexpression influenced cell adhesion, we performed a monocyte adhesion assay. As shown in Fig 1E, the overexpression of miR-3679-5p led to a reduction of monocyte binding to cultured ECs under TNF- α stimulation. Taken together, these results suggested that miR-3679-5p could be a miRNA that potentially regulates adhesion molecules during TNF- α -induced early inflammatory responses in ECs.

Identification of KDM7A and UTX as potential target genes of miR-3679-5p

miRNAs function as gene repressors by complementary base pairing with their target mRNAs within miRNA–mRNA duplexes. Each miRNA has many potential target mRNAs, because its “seed” sequence contains ~6 to ~8 nt (Garcia *et al*, 2011). To identify the

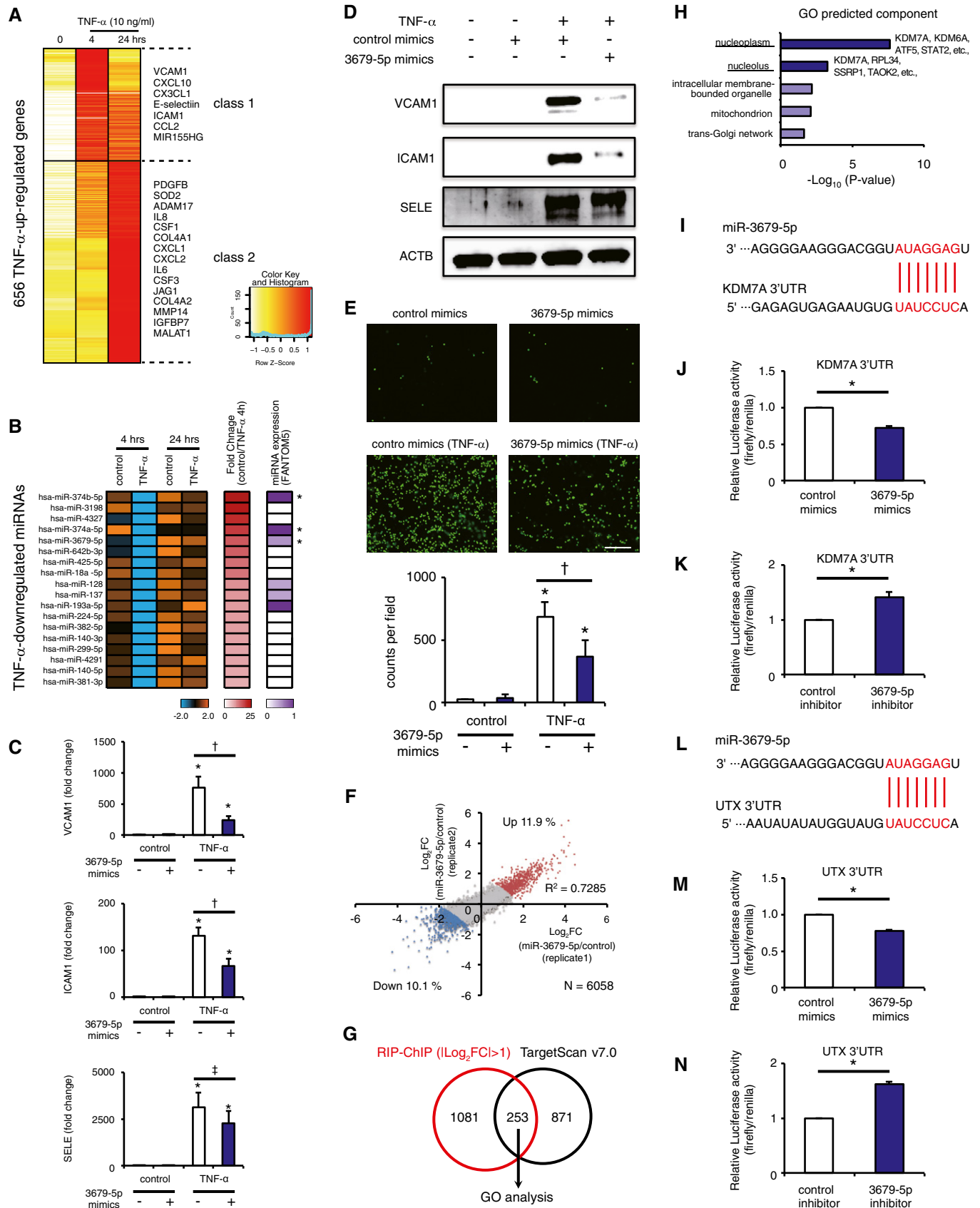


Figure 1.

Figure 1. The novel miR-3679-5p suppresses monocyte adhesion and targets two histone demethylases, KDM7A and UTX, in human inflammatory activated ECs.

- A Heat map representation of the TNF- α -up-regulated genes. Genes were classified based on the TNF- α -treated time points, using the algorithm "HOPACH".
- B Heat map showing down-regulated miRNAs at 4 h, but not 24 h, after TNF- α treatment. The middle column indicates the fold-change values (control/TNF) at 4 h. The right column indicates the relative expression level of each miRNA from the FANTOM5 database (Consortium *et al*, 2014). Asterisks indicate the top three most down-regulated miRNAs which were reported to be expressed in human endothelial cells (ECs) according to the FANTOM5 database.
- C Bar plots showing mean mRNA levels of vascular cell adhesion molecule-1 (VCAM1), intracellular adhesion molecule-1 (ICAM1), and E-selectin (SELE), measured 4 h after stimulation of human ECs with or without TNF- α \pm miR-3679-5p. Data are shown as means \pm SE ($n = 3$). * $P < 0.05$ compared to TNF- α (-) mimics (-). $^{\dagger}P < 0.05$ and $^{\ddagger}P = 0.203$ compared to TNF- α (+) mimics (-). Statistical differences were analyzed by the Tukey–Kramer test.
- D Western blots for VCAM1, ICAM, SELE, and β -actin (ACTB) in lysates from ECs treated with or without TNF- α (4 h) \pm miR-3679-5p.
- E Representative images (top) and bar plot quantification (bottom) showing the adhesion of calcein-labeled U937 monocytes to ECs treated with or without TNF- α \pm miR-3679-5p. Scale bar represents 250 μ m. Graphs are representative of three independent experiments. Data are shown as means \pm SD. * $P < 0.05$ compared to TNF- α (-) mimics (-). $^{\dagger}P < 0.05$ compared to TNF- α (+) mimics (-). Statistical differences were analyzed by the Tukey–Kramer test.
- F The scatter plot shows the correlation of RNA immunoprecipitation (RIP) followed by microarray data from two replicate screens for the identification of miR-3679-5p target genes. Genes up- and down-regulated by miR-3679-5p treatment (average $\text{Log}_2\text{FC} > 1$) are indicated in red and blue, respectively.
- G Venn diagram showing the overlap of the genes selected by RIP-ChIP (1,334) and TargetScan7.0 (1,224) (http://www.targetscan.org/vert_70/).
- H Gene ontology (GO) analysis of the 253 potential target genes for miR-3679-5p, as determined in (G). The P -values of each category analyzed from DAVID (<https://david.ncifcrf.gov/>) are shown in the bar graphs.
- I Seed sequence of miR-3679-5p and complementary 3' UTR sequence of lysine demethylase 7A (KDM7A). The letters in red indicate matched bases.
- J, K Effect of miR-3679-5p mimics (J) or miR-3679-5p inhibitor (K) on luciferase activity in pmirGLO-transfected ECs expressing the 3' UTR of KDM7A. Data are shown as means \pm SE ($n = 3$). * $P < 0.05$ compared to control. Statistical differences were analyzed by the Student's t -test.
- L Seed sequence of miR-3679-5p and complementary 3' UTR sequence of lysine demethylase 6A (UTX). The letters in red indicate matched bases.
- M, N The effect of miR-3679-5p mimics (M) or miR-3679-5p inhibitor (N) on luciferase activity in pmirGLO-transfected ECs expressing the 3' UTR of UTX was measured. Data are shown as means \pm SE ($n = 3$). * $P < 0.05$ compared to control. Statistical differences were analyzed by the Student's t -test.

Source data are available online for this figure.

target mRNAs of miR-3679-5p in human ECs, we performed biologically duplicate RNA immunoprecipitation (RIP)-Chip analyses using an antibody against argonaute 2 (AGO2), an essential component of the RNA-induced silencing complex (RISC). The miRNA that binds to its target mRNA is incorporated into a RISC (Bartel, 2018) and can therefore be co-isolated with an antibody against AGO2. Utilizing this approach, ECs transfected with miR-3679-5p or negative control miRNA mimics were stimulated with TNF- α and subsequently immunoprecipitated with an anti-AGO2 antibody. The AGO2-bound RNAs were subjected to a microarray analysis, and the differentially regulated mRNAs were filtered out (> 2 -fold different between miR-3679-5p and negative control in both replicates), identifying a total of 1,334 probes (Fig 1F and G). To detect the direct target mRNAs, the 1,334 probes were further filtered by the computational algorithm, TargetScan7.0 (Agarwal *et al*, 2015), and 253 genes were identified as bona fide targets for miR-3679-5p (Fig 1G). To fully inspect the functions of these 253 genes, we performed a GO analysis. The most significantly enriched GO term was nucleoplasm, consisting of 66 genes (Fig 1H, $P = 6.22\text{E-}06$ after Benjamini correction). Interestingly, these 66 genes included the two histone demethylases KDM7A and KDM6A (UTX), which modify the methylation levels of histone tails and participate in gene regulation (Agger *et al*, 2007; Lan *et al*, 2007; Tsukada *et al*, 2010). Since we previously reported that histone modification changes of H3K4me1 and H3K4me3 preceded the mRNA induction of genes associated with inflammatory responses in ECs (Tozawa *et al*, 2011), we focused on these two histone modification enzymes in this work. Using qRT-PCR, we found that the expression of KDM7A and UTX in ECs transfected with miR-3679-5p was significantly down-regulated, in comparison with cells transfected with negative control miRNA mimics (fold change relative to control was 0.68 ($P = 0.0001$) and 0.81 ($P = 0.0351$), respectively). Consistently, the 3'UTRs of KDM7A and UTX have seed sequences corresponding to miR-3679-5p (Fig 1I and L). Furthermore, a reporter assay

confirmed that the transfection of mimics and the inhibition of miR-3679-5p suppressed and increased the luciferase activities, respectively, in ECs (Fig 1J, K, M and N), suggesting that KDM7A and UTX are potentially the direct targets of miR-3679-5p.

KDM7A and UTX participate in TNF- α -induced NF- κ B-p65 signaling pathways leading to activation of ECs

To examine whether KDM7A and UTX are involved in the induction of TNF- α -responsive genes and the activation of the NF- κ B pathway, we performed an RNA-seq analysis in KDM7A and UTX knockdown ECs at 4 h after the TNF- α treatment (Appendix Fig S3A–D). The TNF- α -responsive genes were identified as those that were up-regulated by more than 2-fold after TNF- α treatment. We identified a total of 404 genes as TNF- α -responsive genes, of which 123 genes were down-regulated after NF- κ B inhibition by I κ B- α phosphorylation and degradation inhibitor (BAY 11-7,082, < 0.75 -fold versus TNF- α). Since NF- κ B is a master regulator of gene transcription during inflammatory processes and plays a critical role in EC activation (Papantonis *et al*, 2012; Brown *et al*, 2014b), the 123 NF- κ B-dependent genes were further analyzed by clustering their siRNA-treated expression profiles and divided into five clusters (Fig 2A). The siRNA-mediated knockdown of KDM7A down-regulated almost half of the NF- κ B-dependent genes (*e.g.*, VCAM1, CCL2, CXCL2, CXCL3, CX3CL1, IL8, and SOD2), which play important roles in the immune response and cell chemotaxis (class 2, Fig 2A). The siRNA knockdown of UTX down-regulated a small number of NF- κ B-dependent genes, including SELE (class 3, Fig 2A). Several other NF- κ B-dependent genes were down-regulated by either siKDM7A or siUTX (class 1, Fig 2A). Importantly, the simultaneous knockdown of KDM7A and UTX down-regulated a broad range of NF- κ B-dependent genes (Appendix Fig S4A–G). A principal component analysis (PCA) revealed that the expression patterns of BAY 11-7,082- and siKDM7A+siUTX-treated ECs were

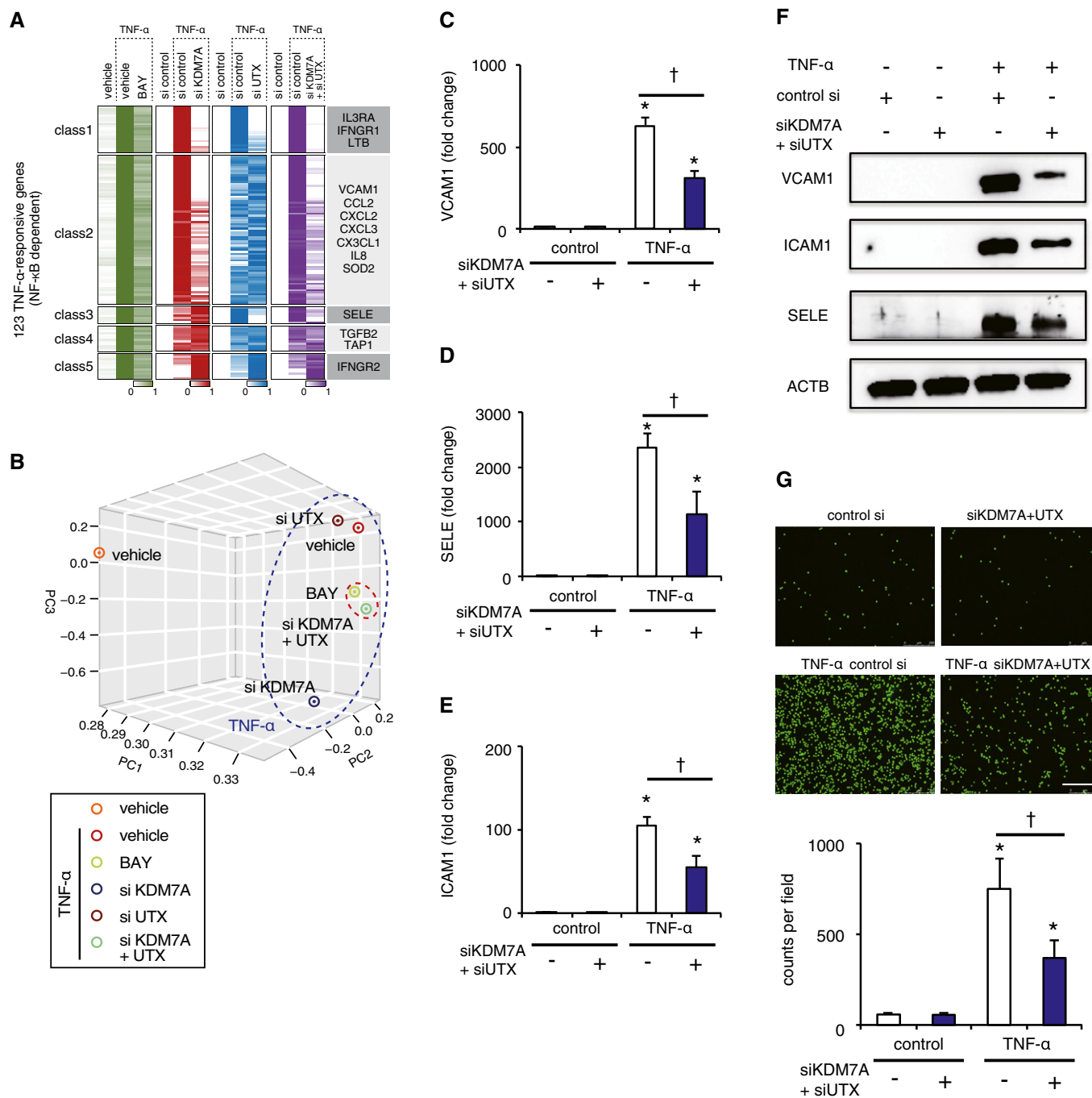


Figure 2. KDM7A and UTX participate in TNF- α -induced NF- κ B-p65 signaling pathways leading to the activation of ECs.

A Heat map representation of RNA-seq results. The p65-dependent genes (total 123; defined as genes up-regulated more than 2-fold via TNF- α treatment and down-regulated more than 0.75-fold via BAY 11–7,082 treatment) were classified based on the alteration patterns by the siRNA knockdown of KDM7A, UTX, and both, using the algorithm “HOPACH”.

B Three-dimensional (3D) multidimensional scaling (MDS) plots. ECs in the presence or absence of TNF- α \pm BAY, siKDM7A, siUTX, or siKDM7A+siUTX were mapped to the 3D space, based on the expression profiles of the TNF- α -responsive genes, by using classical MDS. Each treated cell is represented by a colored dot.

C–E Bar plot showing mean mRNA levels of VCAM1, ICAM1, and SELE measured 4 h after stimulation of ECs with or without TNF- α (siKDM7A+siUTX). Data are shown as means \pm SE ($n = 3$). * $P < 0.05$ compared to TNF- α (-) siKDM7A+siUTX (-). † $P < 0.05$ compared to TNF- α (+) siKDM7A+siUTX (-). Statistical differences were analyzed by the Tukey–Kramer test.

F Western blots for VCAM1, ICAM1, SELE, and ACTB in lysates from ECs treated with or without TNF- α (4 h) \pm (siKDM7A+siUTX).

G Representative images (top) and bar plot quantification (bottom) showing the adhesion of calcein-labeled U937 monocytes to ECs treated with or without TNF- α \pm (siKDM7A+siUTX). Scale bar represents 250 μ m. Graphs are representative of three independent experiments. Data are shown as means \pm SD. * $P < 0.05$ compared to TNF- α (-) siKDM7A+siUTX (-). † $P < 0.05$ compared to TNF- α (+) siKDM7A+siUTX (-). Statistical differences were analyzed by the Tukey–Kramer test.

Source data are available online for this figure.

similar (Fig 2B). Collectively, these transcriptome analyses demonstrated that KDM7A and UTX play critical roles in the TNF- α -induced NF- κ B pathways independently, but have a partial complementary effect in inflammatory ECs.

We next investigated whether KDM7A and UTX are actually involved in the monocyte adhesion of TNF- α -activated ECs. Consistent with the RNA-seq results (Fig 2A), the siKDM7A treatment significantly decreased the TNF- α -induced expression of VCAM1, but not SELE (Appendix Fig S5A–E). In contrast, the knockdown of UTX significantly decreased the TNF- α -induced expression of SELE, but not VCAM1 (Appendix Fig S3G–K). Notably, the simultaneous knockdown of KDM7A and UTX resulted in a significant reduction in the TNF- α -induced expression of VCAM1, ICAM1, and SELE, which led to the inhibition of monocyte adhesion to ECs (Fig 2C–G, Appendix Fig S3F and L). To ensure that the inhibitory effect of adhesion molecule gene expression by the KDM7A and UTX knockdown was not a consequence of the transfection itself or off-target effects, we tested another set of siKDM7A and siUTX oligos and confirmed the reproducible results (Appendix Fig S6A–H). Together, these data suggested that the miR-3679-5p target genes KDM7A and UTX are involved in monocyte adhesion to TNF- α -activated ECs by controlling the expression of adhesion molecules, VCAM1, ICAM1, and SELE.

KDM7A and UTX recruitments coincide with the NF- κ B-p65-related region

Since KDM7A and UTX demethylate H3K9me2 and H3K27me3, respectively, these two factors epigenetically activate their binding loci (Lan *et al*, 2007; Tsukada *et al*, 2010). Given that ablated KDM7A and UTX expression caused transcriptional repression of inflammation-related genes, including adhesion molecules (Fig 2A), we hypothesized that these loci were epigenetically repressed and rapidly activated after TNF- α -stimuli. To test this hypothesis, we performed chromatin immunoprecipitation followed by NGS (ChIP-seq) experiments in replicates, to determine the KDM7A and UTX binding sites before and 1 h after TNF- α stimulation. Since we could not obtain good antibodies against KDM7A and UTX for ChIP, we overexpressed FLAG-tagged KDM7A and UTX, and immunoprecipitated the proteins with anti-FLAG antibodies (Appendix Fig S7A).

Examples of biological replicates and correlations are depicted in Appendix Fig S7B and C. To correlate KDM7A and UTX binding with epigenetic modifications and transcription factor occupancy, we also measured H3K27ac and NF- κ B-p65 at the baseline and after 1 h of TNF- α stimulation. As a result, the TNF- α -inflammatory signal caused rapid and global redistribution of KDM7A, from 1,714 to 2,483 binding regions. Similarly, we identified 1,303 and 933 UTX-associated regions in resting and inflammatory ECs, respectively. In TNF- α -stimulated ECs, the enrichment of KDM7A, UTX, and p65 was evident at promoters (KDM7A: 30.2%, UTX: 20.1%, p65: 20.1%), intragenic regions (KDM7A: 49.6%, UTX: 43.9%, p65: 47.3%), and intergenic regions (KDM7A: 20.2%, UTX: 36.0%, p65: 32.6%) (Fig EV2A, and Appendix Fig S7D). In response to TNF- α , KDM7A and UTX binding was increased in many TNF- α -up-regulated genes, including important adhesion molecules and chemokines, as confirmed by an integrative analysis combined with the RNA-seq and ChIP-seq signal ratios (Fig 3A and B). In accordance with the RNA-seq results (Fig 2A and B), KDM7A bound a larger number of TNF- α -up-regulated genes than UTX (KDM7A: 66, UTX: 33). In contrast, KDM7A and UTX binding was decreased in TNF- α -down-regulated genes mainly related to developmental pathways (Fig 3A and B). Consistently, an analysis with the Genomic Regions Enrichment of Annotations Tool (GREAT) demonstrated that the regions with gains of KDM7A or UTX peaks in TNF- α -stimulated ECs showed enrichment for inflammatory pathways including NF- κ B and TNF receptor signaling, while the regions with a loss of their peaks showed enrichment for important developmental pathways, including Notch and Wnt signaling (Table EV1). For example, the upper right parts of Fig 3A and B include VCAM1, SELE, IL8, and CCL2. In contrast, the lower left parts include SOX18 and BMP4. At the coding gene locations, KDM7A and UTX occupancies around the gene body were increased in TNF- α -up-regulated genes and decreased in TNF- α -down-regulated genes after TNF- α treatment (Figs 3C and D, and EV3A–D). These results demonstrated that the genes with expression that is either up- or down-regulated by TNF- α signaling showed increased and decreased occupancies of the two histone modification enzymes, respectively.

To further examine the characteristics of the KDM7A and UTX binding sites, we performed a motif analysis and found that RELA

Figure 3. ChIP-seq revealing the recruitment of KDM7A and UTX to NF- κ B-p65 related elements.

- A, B Scatter plots showing the connection between KDM7A or UTX binding and RNA expression in TNF- α -stimulated ECs. The X and Y axes indicate the log₂ ratio of fragments per kilobase of exon per million mapped sequence reads (FPKM) values and the ChIP-seq signals (TNF- α 60 min/0 min) for KDM7A (A) and UTX (B), respectively. Genes with more than a 1.5-fold increase in FPKM values (light red dots) satisfying a 0.5-fold increase in ChIP-seq signals are indicated as dark red dots. Genes with a 1.5-fold decrease in FPKM values (light blue dots) satisfying a 0.5-fold decrease in ChIP-seq signals are indicated as dark blue dots. These genes are defined as the target genes for KDM7A (A) and UTX (B), respectively. The names of representative genes are shown in the graphs.
- C, D Metagene representations of KDM7A (C) and UTX (D) ChIP-seq signals in units of read count per million mapped reads at a meta composite of the genomic regions around the TNF- α -up-regulated genes.
- E *De novo* motif analyses for KDM7A (top) and UTX (bottom) binding recognition sequences in TNF- α -stimulated ECs. The *P*-value indicates significant enrichment of the transcription factor binding motif in KDM7A/UTX binding sites, in comparison to a size-matched random background.
- F Heat map of H3K27ac (green), p65 (yellow), KDM7A (red), and UTX (purple) levels in resting and TNF- α -stimulated ECs. Each row shows \pm 10 kb centered on the KDM7A (top) or UTX (bottom) peak. Rows are ordered by max KDM7A or UTX signal in each region. The ChIP-seq signal is depicted by color scaled intensities.
- G, H Gene tracks of ChIP-seq signals for H3K27Ac, p65, KDM7A, and UTX, and RNA-seq signals around the VCAM1 (G) and SELE (H) loci in TNF- α (–) and TNF- α (+) ECs. ChIP-seq and RNA-seq signals are visualized by Integrated Genome Viewer (<http://software.broadinstitute.org/software/igv/>).
- I, J ChIP-qPCR of p65 (I) and KDM7A (J) at the VCAM1 TSS, normalized to input. Graphs are representative of three independent experiments. Data are shown as means \pm SD. **P* < 0.05 compared to TNF- α (–). †*P* < 0.05 compared to TNF- α (+) siKDM7A (–). Statistical differences were analyzed by the Tukey–Kramer test.
- K, L ChIP-qPCR of p65 (K) and UTX (L) at the SELE TSS, normalized to input. Graphs are representative of three independent experiments. Data are shown as means \pm SD. **P* < 0.05 compared to TNF- α (–). Statistical differences were analyzed by the Tukey–Kramer test.

Source data are available online for this figure.

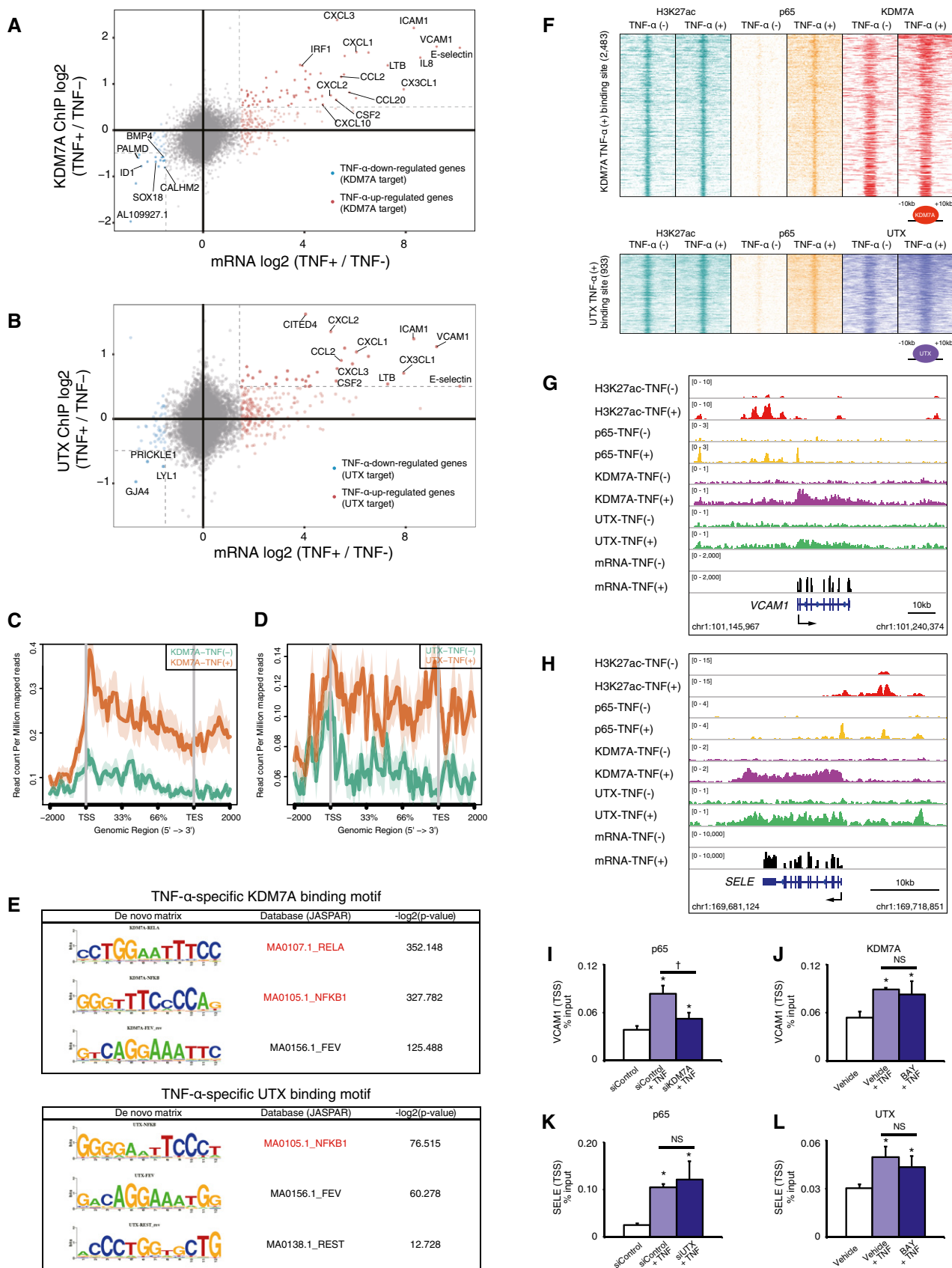


Figure 3.

(NF- κ B-p65) and NFKB1 (NF- κ B-p105) binding sequences were significantly enriched, as compared with random genomic background sequences (Fig 3E). The co-localization of KDM7A/UTX and p65 was also confirmed by peak density heat maps (Fig 3F). From the perspective of p65 binding sites, we identified the recruitment of substantial levels of KDM7A and UTX (Fig EV2B and C). At the *VCAM1* locus, TNF- α stimulation of ECs for 1 h increased p65, KDM7A, and UTX occupancy at promoters and surrounding enhancer-like elements marked by H3K27ac (Fig 3G). Coincident with these observations, comparable evidence was obtained at the *SELE* locus, where TNF- α treatment recruited both KDM7A and UTX to the promoter and enhancer-like elements co-localized with p65 (Fig 3H). It should be noted that KDM7A and UTX were bound to the gene bodies of *VCAM1* and *SELE*. Taken together, these results suggested that KDM7A and UTX are recruited to NF- κ B-p65-related regions and contribute to transcriptional control through TNF- α signaling in ECs.

Although the interplay between epigenetic mediators and transcription factors is crucial for cytokine signal transduction, it is unclear which factor works upstream from the other. Previous studies hinted that the interplay might depend on the cellular environment or the nuclear architecture (Heinz *et al*, 2015). To examine the temporal relationships between p65 and KDM7A/UTX recruitment to regulatory elements in this context, we performed siRNA experiments for KDM7A and UTX, followed by ChIP-qPCR for p65 enrichment. As shown in Fig 3I, the knockdown of KDM7A reduced the TNF- α -induced enrichment of p65 at the *VCAM1* transcription start site (TSS). However, the BAY 11–7,082 treatment did not affect the recruitment of KDM7A at the *VCAM1* TSS (Fig 3J). At the *SELE* TSS, the knockdown of UTX and the BAY 11–7,082 treatment had no effect on the recruitment of p65 and UTX, respectively (Fig 3K and L). Thus, KDM7A, but not UTX, might be required for the TNF- α -induced recruitment of p65 to regulatory elements in ECs.

TNF- α immediately removes H3K9me2 and H3K27me3 marks around KDM7A- and UTX-target genes

The KDM7A and UTX mediated demethylation of repressive histone marks (H3K9me2 and H3K27me3, respectively) correlates with active gene expression (Agger *et al*, 2007; Lee *et al*, 2007;

Tsukada *et al*, 2010). Therefore, we hypothesized that the transcriptional activation of genes in TNF- α -stimulated ECs would involve KDM7A and UTX dependent histone modifications. To address this hypothesis, we examined the epigenetic landscape for H3K9me2 and H3K27me3 in ECs after TNF- α signaling by ChIP-seq. As shown in Fig 4A and B, the ChIP-seq signals for H3K9me2 and H3K27me3 around important adhesion molecules and chemokines were immediately decreased in response to TNF- α treatment, although the global levels of H3K9me2 and H3K27me3 around KDM7A and UTX target genes remain unchanged. At the *VCAM1* locus, the ChIP-seq signals for H3K9me2 were broadly decreased 1 h after TNF- α treatment, which coincides with KDM7A recruitment (Fig 4C). ChIP followed by qPCR also revealed a significant reduction in H3K9me2 levels around the TSS and enhancer regions of *VCAM1* (Fig 4D). We observed reduction in ChIP-seq signals for H3K27me3 around the upstream enhancer regions of the *VCAM1* locus. In consistent with this, ChIP followed by qPCR detected a significant reduction of H3K27me3 especially within the enhancer regions, but not the TSS (Fig 4C and E). Similarly, at the *SELE* locus, the H3K9me2 and H3K27me3 levels detected by ChIP-seq and ChIP-qPCR were broadly decreased in association with KDM7A and UTX recruitment in both the TSS and enhancer regions (Fig 4F–H). In contrast, TNF- α treatment did not affect the H3K9me2 and H3K27me3 levels at the genomic regions of *HOXA13* and *GATA4*, which are not or only weakly expressed in human ECs with or without an exogenous stimulus (Fig 4I and J; Kanki *et al*, 2011). Next, to test whether the repressive histone mark reduction rapidly induced by TNF- α stimulation was directly due to the two histone modifiers, we further assessed the influence of the knockdowns of KDM7A and UTX on the H3K9me2 and H3K27me3 levels in the genomic regions around *VCAM1* and *SELE*, respectively. The siRNA knockdowns of KDM7A and UTX restored H3K9me2 and H3K27me3 at representative regions of *VCAM1* and *SELE*, respectively, in TNF- α -treated human ECs (Fig 4K and L). Taken together, these results suggested that the KDM7A and UTX mediated regulation of repressive histone marks might be a key mechanism for the transcriptional activation of inflammatory genes in human ECs.

Figure 4. H3K9me2 and H3K27me3 marks around KDM7A- and UTX-target genes change after TNF- α treatment.

- A, B Boxplots of the log₂ fold change of ChIP-seq enrichment of H3K9me2 in KDM7A target genes (A) and that of H3K27me3 in UTX-target genes (B) with TNF- α treatment (TNF⁺) and control (TNF⁻). The horizontal line within the box represents the median sample value. The ends of the box represent the 3rd and 1st quartiles. The whiskers extend from the ends of the box to the outermost data point that falls within the distances computed as follows: 3rd quartile +1.5* (interquartile range) and 1st quartile –1.5*(interquartile range). Each dot in the box plot shows data for one single target gene. Genes colored red represent the top five down-regulated target genes with TNF- α -treatment, as compared to control. Graphs are representative of two independent experiments.
- C Gene tracks of ChIP-seq signals for H3K9me2 and H3K27me3 around the *VCAM1* locus in TNF- α (–) and TNF- α (+) ECs.
- D, E ChIP-qPCR showing enrichment (percent input) of H3K9me2 (D) and H3K27me3 (E) around the *VCAM1* locus. Primer pairs targeting distinct regions are listed on the X-axis. Graphs are representative of three independent experiments. Data are shown as means \pm SD. **P* < 0.05 compared to TNF- α (–). Statistical differences were analyzed by the Student's *t*-test.
- F Gene tracks of ChIP-seq signals for H3K9me2 and H3K27me3 around the *SELE* locus in TNF- α (–) and TNF- α (+) ECs.
- G, H ChIP-qPCR showing enrichment (percent input) of H3K9me2 (G) and H3K27me3 (H) around the *SELE* locus. Primer pairs targeting distinct regions are listed on the X-axis. Graphs are representative of three independent experiments. Data are shown as means \pm SD. **P* < 0.05 compared to TNF- α (–). Statistical differences were analyzed by the Student's *t*-test.
- I, J ChIP-qPCR showing enrichment (percent input) of H3K9me2 and H3K27me3 around the *HOXA13* (I) and *GATA4* (J) loci. Graphs are representative of three independent experiments. Data are shown as means \pm SD. **P* < 0.05 compared to TNF- α (–). Statistical differences were analyzed by the Student's *t*-test.
- K, L ChIP-qPCR showing enrichment (percent input) of H3K9me2 around *VCAM1* –11 kb (K) and H3K27me3 around *SELE* –12 kb (L). Graphs are representative of three independent experiments. Data are shown as means \pm SD. **P* < 0.05 compared to TNF- α (–). †*P* < 0.05 compared to TNF- α (+) siKDM7A (–) or TNF- α (+) siUTX (–). Statistical differences were analyzed by the Tukey–Kramer test.

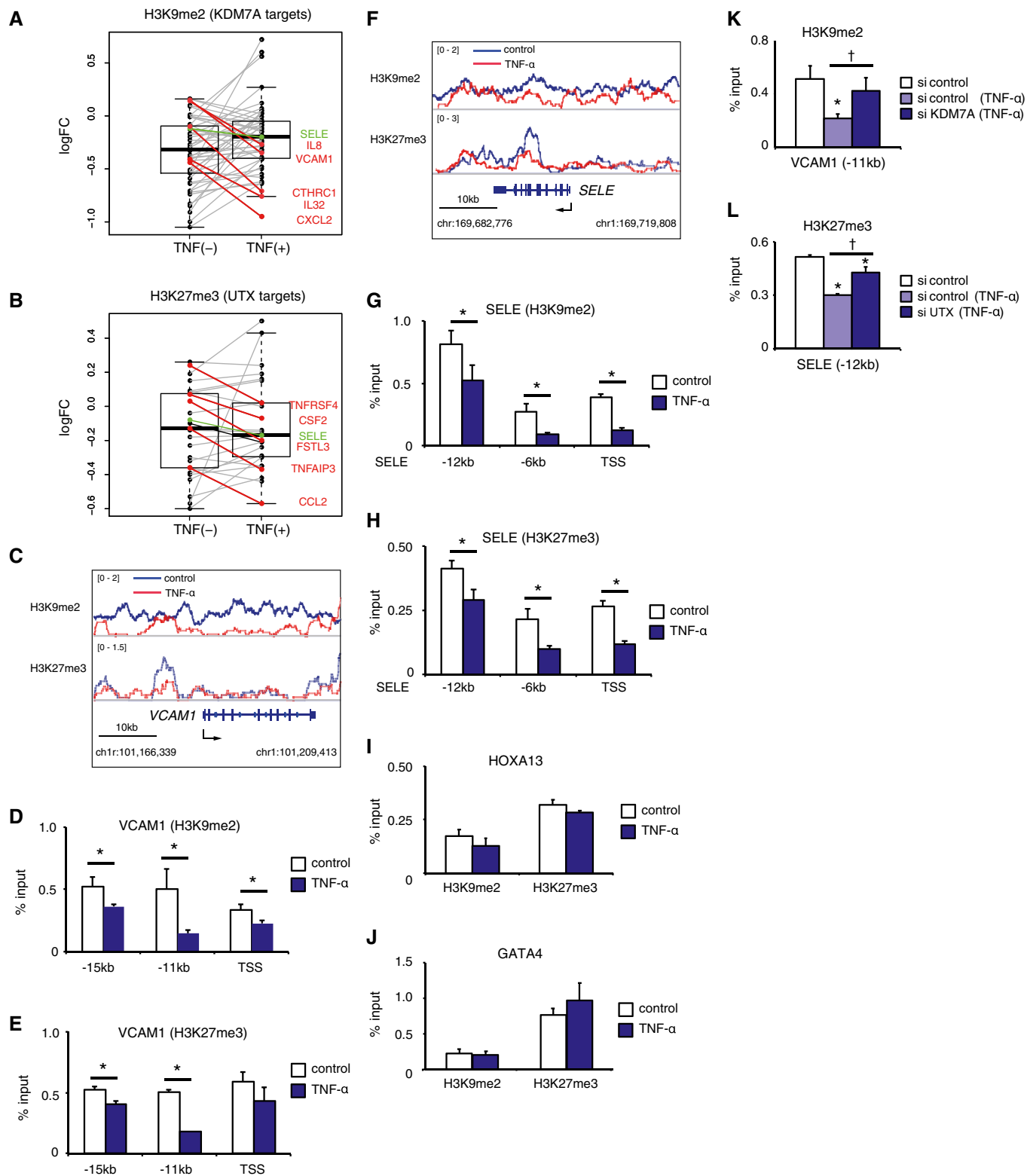


Figure 4.

TNF- α -induced SEs correlate with KDM7A and UTX recruitment and chromatin conformation change

SEs are genomic regions consisting of clusters of regulatory elements bound with extremely high amounts of transcription

factors and are associated with characteristic histone modifications and genomic architecture. Recent studies have shown that the interaction between NF- κ B-p65 and BRD4 on SEs rewires the gene expression program toward proinflammatory responses in human ECs. We found that the ChIP-seq signals for BRD4 (Brown *et al*,

2014b; Data ref: Brown *et al*, 2014a) and H3K27ac increased at the KDM7A and UTX binding sites in TNF- α -treated human ECs (Appendix Fig S8A and B). Thus, we hypothesized that the recruitment of KDM7A and UTX was coincident with and functionally associated with TNF- α -induced SEs. To test this hypothesis, we used ROSE (Whyte *et al*, 2013) and defined the SEs in human ECs based on the ChIP-seq signals for BRD4 (Brown *et al*, 2014b; Data ref: Brown *et al*, 2014a). When ranked by increasing BRD4 enrichment, 311 and 356 SEs were identified in resting (TNF- α -untreated) and TNF- α -treated ECs, respectively. Many of these SEs are identical to the KDM7A and UTX bound regions (Figs 5A and EV4A). These identical SEs in TNF- α -treated ECs were located adjacent to inflammatory gene loci, including *VCAM1*, *IL8*, *SELE*, and *CCL2*, while those in resting ECs were located adjacent to gene loci critical to non-inflammatory EC functions, such as *SOX18*, *NR2F2*, *ESAM*, and *PECAM1*. Furthermore, as compared to typical enhancers (TEs: obtained from the pre-compiled HUVEC ngspilotdb), KDM7A and UTX binding was dramatically increased at SEs (Fig 5B and C). These results indicated the possible roles of KDM7A and UTX in the function or formation of SEs in human ECs.

The relationship between SEs and genomic architecture has been implicated, especially in stem cells and cancer cells, by mapping the local chromosomal structure using ChIA-PET (Handoko *et al*, 2011; Downen *et al*, 2014; Hnisz *et al*, 2016). To capture the active formation of chromatin loops through TNF- α signaling in human ECs, we performed ChIA-PET using an antibody against the phospho-Ser2/Ser5 heptad repeats in the C-terminus of the largest catalytic subunit of RNA polymerase II (active RNAP). The active RNAP ChIA-PET data identified 5,948,648, 4,849,886, and 3,893,377 interactions at 0, 30, and 60 min after the TNF- α treatment, respectively, suggesting that the active RNAP interactions slightly decreased overall but were concentrated on specific inflammatory response loci. These ChIA-PET data were further processed by the ChIA-PET tools (Li *et al*, 2010), which identified an average of 4,280 high-confidence interactions (false discovery rate of 1% and $P < 0.0001$), including 159 SE-SE interactions. The SE-SE loops had a median length of 7,023 bp. We next investigated whether the SE-SE interactions could be changed upon TNF- α stimulation in human ECs. We compared the ChIA-PET interaction changes between control-specific, common, and TNF- α -specific SEs. Interestingly, the ChIA-PET interactions increased at TNF- α -specific SEs in response to TNF- α , while they decreased at control-specific SEs (Fig 5D). Importantly, the ChIA-PET interactions

increased at both the KDM7A and UTX binding sites in TNF- α -treated ECs (Fig 5E and F). As shown in Fig 5G and H, the SE-SE interactions were newly formed within 1 h after TNF- α treatment at the *VCAM1* and *IL8* loci, and were associated with the recruitment of KDM7A and UTX. In contrast, in response to TNF- α , the ChIA-PET interactions decreased at the loci of genes critical for EC function, such as *SOX18* and *NR2F2*, in conjunction with decreased transcription and KDM7A and UTX recruitment (Fig EV4B and C). As exemplified by the *VCAM1*, *IL8*, and *SELE* loci, the H3K9me2 and H3K27me3 levels decreased at SEs in TNF- α -treated human ECs (Fig 5I–K). Collectively, these data suggested that KDM7A and UTX might be functionally involved in the formation of SEs and the chromosomal conformation changes activating their associated genes during early inflammatory responses in human ECs.

TNF- α immediately induces chromosomal conformation changes within sub-TADs in human ECs

Although the active RNAP ChIA-PET data indicated that chromosomal conformation changes immediately occurred after TNF- α treatment in human ECs, the ChIA-PET analysis was methodologically biased by the factor-dependent immunoprecipitation step and therefore could not directly reflect the chromosomal conformation changes. To address this point, we performed *in situ* Hi-C, which allows the unbiased identification of chromatin interactions across an entire genome. We obtained a total of approximately 200 million reads from two biological replicates under each condition (*i.e.*, TNF- α 0 min: replicate 1, replicate 2, and TNF- α 60 min: replicate 1, replicate 2). Since the two biological replicates showed a high degree of correlation (Appendix Fig S9A and B), the Hi-C data from the two biological replicates were combined for further analysis. We detected 10,577 and 10,851 interactions in the TNF- α -untreated and TNF- α -treated human ECs, respectively, among which 7,196 interactions were shared. The Hi-C matrix identified megabase size TADs with boundaries that were highly similar between the TNF- α -untreated and TNF- α -treated human ECs (Fig EV5A and B). Indeed, the total number of TADs, which was calculated by TADtool (Kruse *et al*, 2016), remained relatively unchanged before (6,349) and after (7,103) TNF- α treatment. Importantly, this is consistent with previous reports showing that megabase size TADs are largely conserved among different tissues, and are already formed in embryonic stem cells and remain relatively constant during development (Dixon *et al*, 2012).

Figure 5. The recruitment of KDM7A and UTX is associated with the formation of TNF- α -induced SEs and their associated chromatin loop formation.

- A Plot of enhancers defined in TNF- α -treated ECs, ranked by increasing bromodomain-containing protein 4 (BRD4) signal. Super enhancers (SEs) were defined by ROSE (Loven *et al*, 2013; Whyte *et al*, 2013), based on the ChIP-Seq signals for BRD4 (Brown *et al*, 2014b). SEs are indicated by dashed lines and are colored yellow. The numbers show the total SEs and their classification based on KDM7A and UTX binding. Representative SE-related genes are indicated in the graph.
- B, C Metagene representations of KDM7A (B) and UTX (C) ChIP-seq signals in units of read count per million mapped reads, at a meta composite of SEs and typical enhancers (TEs). TEs were obtained from the pre-compiled HUVEC ngspilotdb (<https://github.com/shenlab-sinai/ngspilot>).
- D Pirate plots showing ChIA-PET interaction changes at control-specific, common, and TNF- α -specific SEs. The Y-axis indicates the log₂ ratio of ChIA-PET signals (TNF- α 60 min/0 min). The central bar indicates the average.
- E, F Bean plots showing ChIA-PET interaction changes at KDM7A (E) and UTX (F) binding sites. The Y-axis indicates the log₂ ratio of ChIA-PET signals (TNF- α 60 min/0 min). The central bar indicates the median.
- G, H ChIA-PET interactions of active RNA pol II around the *VCAM1* (G) and *IL8* (H) loci integrated with the ChIP-seq profiles of KDM7A, UTX, and BRD4, and RNA-seq profiles in TNF- α (–) and TNF- α (+) ECs. ChIA-PET interactions were visualized by the WashU Epigenome Browser (<http://epigenomegateway.wustl.edu/browser/>). Interactions detected by ChIA-PET are depicted with purple lines. Red bars show TNF- α -specific SEs.
- I–K Gene tracks of ChIP-seq signals for H3K9me2 and H3K27me3 around *VCAM1* (I), *IL8* (J), and *SELE* (K) in TNF- α (–) and TNF- α (+) ECs. Red bars show TNF- α -specific SEs.

Source data are available online for this figure.

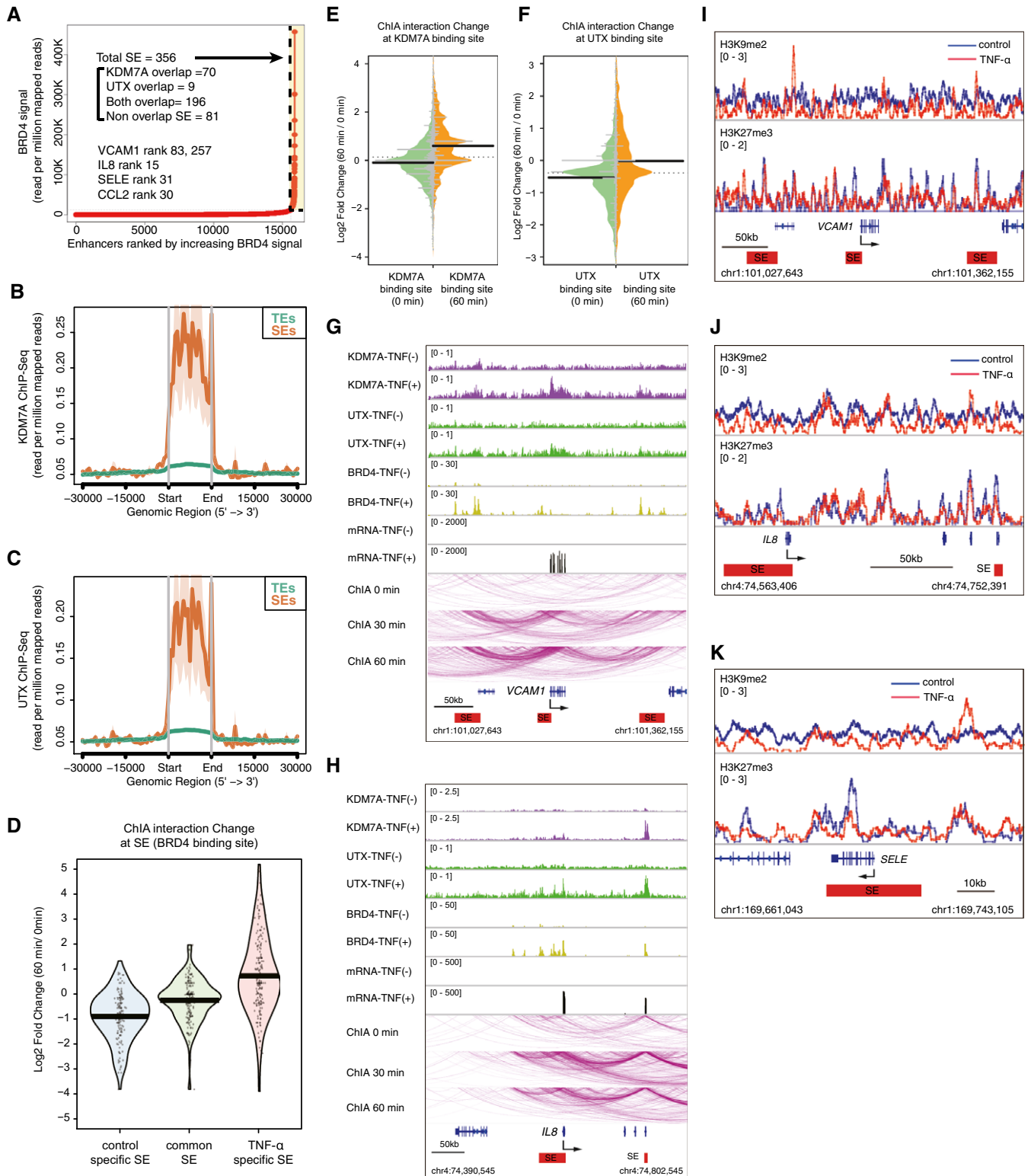


Figure 5.

Since the SEs and their associated genes are located within sub-TAD boundaries (~1 Mb) (Downe *et al.*, 2014; Tang *et al.*, 2015), we further analyzed the “intra-TAD” interactions occurring within sub-TADs. Virtual 4C, derived from Hi-C data at the representative *VCAM1*

and *IL8* loci, showed an increase of several SE-SE interactions within 1 h after TNF-α treatment in human ECs (Fig EV5C and D). Accordingly, HiCCUPS, an algorithm for finding chromatin loops (Rao *et al.*, 2014), identified newly formed SE-SE loops in TNF-α-treated human

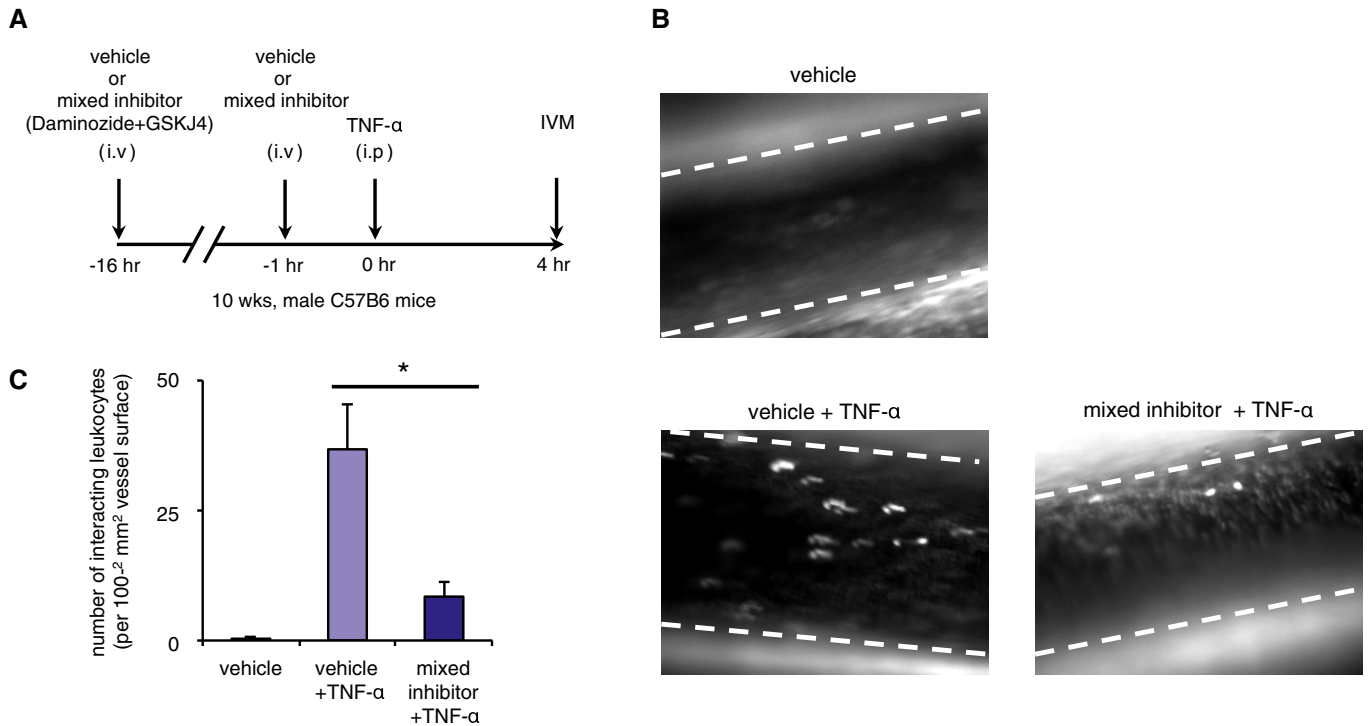


Figure 6. KDM7A and UTX are important for leukocyte adhesion in mice.

A Drug administration protocol for intravital microscopy (IVM) experiments. Male, 10-week-old C57BL/6 mice ($n = 3/\text{group}$) were pretreated with vehicle or mixed inhibitor (Daminiozide+GSKJ4, 50 mg/kg each) at 16 h and 1 h prior to TNF- α treatment. Inflammation was induced by an intraperitoneal injection of TNF- α (5 $\mu\text{g}/\text{mouse}$), and IVM was performed 4 h later.

B Representative snapshot from the IVM analysis of leukocyte adhesive interactions in the femoral arteries. Margins of vessels are indicated with dashed lines. White spots represent fluorescently labeled leukocytes visualized by the intravenous injection of rhodamine 6G.

C Quantitative analyses of leukocyte adhesive interactions in the femoral arteries. Data are shown as means \pm SE ($n = 3/\text{group}$). * $P < 0.05$ compared to the vehicle + TNF- α group. Statistical differences were analyzed by the Student's t -test. See also Movies EV1 and EV2.

ECs around the genomic regions of *VCAM1* (2 loops) and *IL8* (1 loop) (Fig EV5C and D). Importantly, these newly formed SE-SE loops were located within sub-TADs, which were similar before and after the TNF- α treatment in human ECs. In addition, the Aggregate Peak Analysis (APA) (Rao *et al*, 2014) revealed that the loops only found in TNF- α -treated ECs were strengthened by TNF- α signaling (1.12–2.38 or 0.58–2.29 at *VCAM1* SEs, 1.99–3.16 at *IL8* SEs) (Fig EV5C and D). In contrast, the Hi-C interactions were unchanged at the genomic regions of the *PALMD* and *HOXA* loci, which exist beside the control-specific and common SEs, respectively (Appendix Fig S10A and B). Taken together, these data indicated that the chromosomal conformation changes within sub-TADs could occur at the active transcriptional regions during the early inflammatory response in human ECs.

KDM7A and UTX are important for leukocyte adhesion in mice

Recent studies demonstrated the utilities of the KDM2/7 subfamily inhibitor Daminiozide and the KDM6 subfamily inhibitor GSK-J4 for treating breast cancer and brainstem glioma, respectively (Hashizume *et al*, 2014; Chen *et al*, 2016). To explore the phenotypic effects of the pharmacological inhibition of KDM7A and UTX, we tested the functional effects of Daminiozide and GSK-J4 on leukocyte rolling across TNF- α -activated endothelium *in vivo*. C57BL/6 mice were pretreated with Daminiozide alone (50 mg/kg), GSK-J4 alone

(50 mg/kg), or Daminiozide in combination with GSK-J4 (50 mg/kg each) at 16 h and 1 h prior to TNF- α injection (Fig 6A). The leukocyte adhesive interaction in the left femoral artery was observed by intravital microscopy, which showed that Daminiozide in combination with GSK-J4 significantly decreased the number of interacting leukocytes induced by TNF- α -injection (36.7 versus 8.4, $P < 0.05$; Fig 6B and C). Importantly, Daminiozide alone and GSK-J4 alone did not improve the leukocyte adhesive interactions (Appendix Fig S11A and B), suggesting that KDM7A and UTX are cooperatively involved in endothelium activation in mice.

Discussion

The inflammatory response plays an important role in tissue homeostasis and its dysregulation underlies numerous diseases (Libby, 2002; Libby *et al*, 2011; Gistera & Hansson, 2017), and thus, it is crucial to understand how these processes are regulated. The master transcription factor, NF- κ B, directly controls the induction of a very large fraction of inflammatory genes (Zhang *et al*, 2017). Recent genome-wide studies in differentiated cells have revealed the essential role of epigenetic regulation in orchestrating the information from an inflammatory cascade to regulate NF- κ B recruitment to specific genomic sites and activate NF- κ B-dependent gene

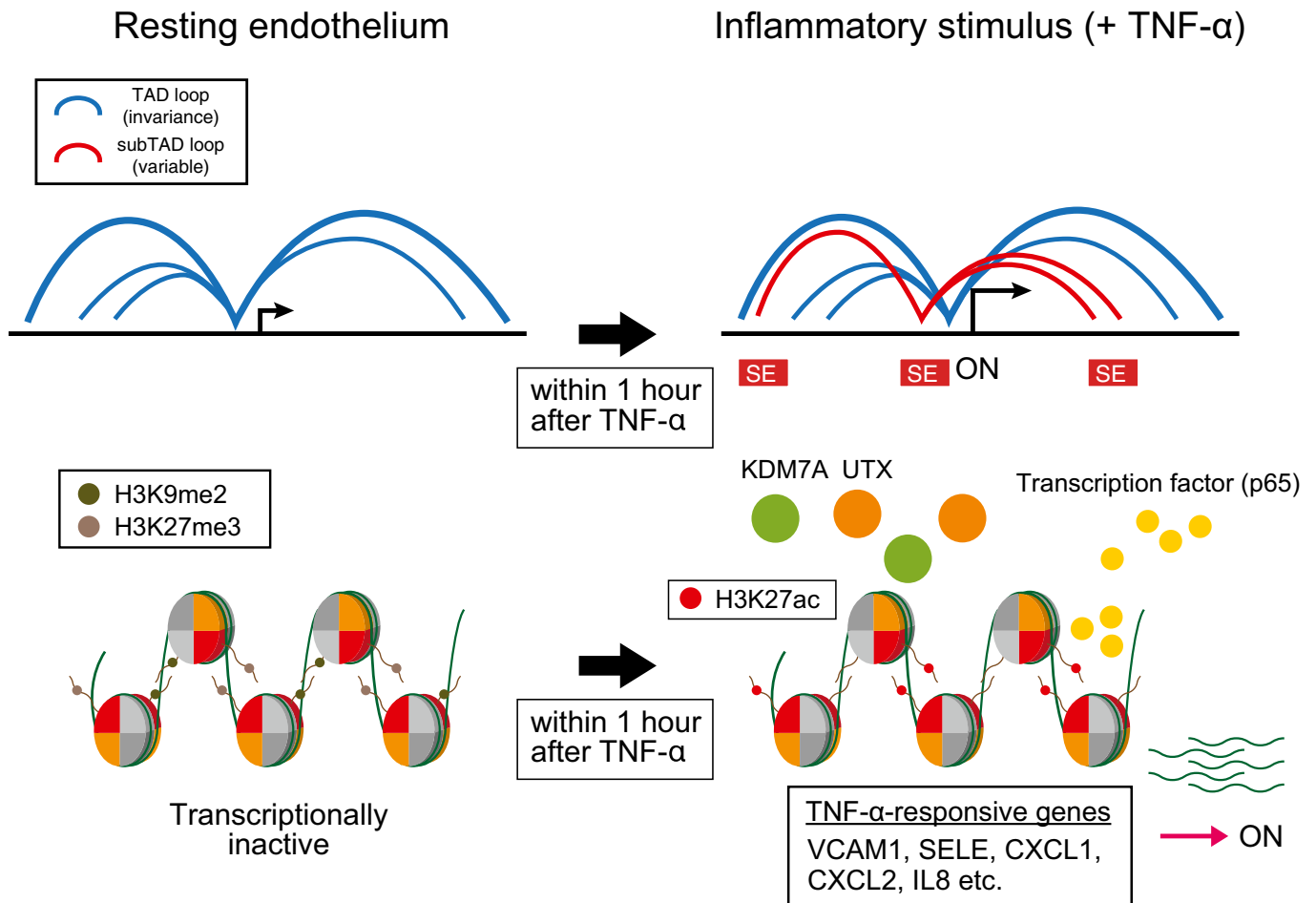


Figure 7. A schematic model of epigenetic changes during TNF- α -induced EC activation.

expression programs. In human ECs, about half of the NF- κ B-bound enhancers are pre-bound by both the ETS and AP1 transcription factors (Hogan *et al*, 2017), and the activation of human ECs with TNF- α results in the formation of large NF- κ B-bound enhancer clusters (*i.e.*, SEs), which are highly occupied by BRD4 and a driving force for activating proinflammatory gene expression (Brown *et al*, 2014b). However, the current comprehension of the epigenetic mechanisms that govern transcriptional activation during early inflammatory responses is far from complete. Here, we demonstrated the intrinsic and synergistic roles of two histone demethylases, KDM7A and UTX, in regulating the epigenetic landscape and the inflammatory gene expression program through the TNF- α /NF- κ B signaling pathway in human ECs.

An early study showed the rapid demethylation of H3K9 (the antibody used in this study did not seem to discern the mono-, di-, or tri-methyl state of H3K9) at promoters of activated inflammatory genes in macrophages treated with lipopolysaccharide (LPS) (Sacconi & Natoli, 2002). Other work demonstrated the important role for H3K9me2 in the regulation of cytokine expression, which was confirmed by findings of lower levels of H3K9me2 at inflammatory gene promoters in innate immune cells as compared with nonimmune cells, such as mouse embryonic fibroblasts and cardiomyocytes. Genetic deletion and pharmacological inhibition of the

H3K9 methyltransferase G9a resulted in the phenotypic conversion of fibroblasts into highly potent cytokine-producing cells (Fang *et al*, 2012). It was also reported that the expression levels of the H3K27 demethylase JMJD3 were increased in mouse macrophages dependent on NF- κ B, in response to LPS (De Santa *et al*, 2007). GSK-J4, a potent enzyme inhibitor of JMJD3 and UTX, reduced LPS-induced proinflammatory cytokine production in human primary macrophages, and this was associated with the retention of H3K27me3 at inflammatory gene loci (Kruidenier *et al*, 2012). In this study, we found that KDM7A and UTX regulate the expression of many NF- κ B-dependent genes in TNF- α -treated human ECs. KDM7A and UTX were rapidly recruited to the loci of inflammatory genes in human ECs in response to TNF- α , and this was highly correlated with NF- κ B binding. We also observed that TNF- α stimulation decreased the H3K9me2 and H3K27me3 levels at the target gene loci of KDM7A and UTX, respectively. As typical examples, the H3K9me2 levels at the *VCAM1* locus and the H3K27me3 levels at the *SELE* locus were retained by the knockdowns of KDM7A and UTX, respectively, in TNF- α -treated human ECs. Taken together, our data have identified KDM7A and UTX as previously unknown histone lysine demethylases that influence the transcription of inflammatory genes through TNF- α signaling in human ECs.

Our results have demonstrated that KDM7A and UTX control large and small numbers of NF- κ B-dependent genes, respectively, in TNF- α -treated human ECs. This is consistent with the results that KDM7A is recruited to many more TNF- α -induced gene loci than UTX. Thus, in comparison with UTX, KDM7A seems to play a dominant role for regulating inflammatory responses in human ECs. In line with this, recent studies have demonstrated that genes involved in immune responses were more likely targeted by H3K9me2 than H3K27me3 during early mouse development (Zylicz *et al*, 2015) and UTX H3K27me3 demethylase activity might not be required for conversion of inactive enhancer in mouse ESCs to active enhancer during differentiation (Wang *et al*, 2017). Importantly, some inflammatory genes, including ICAM1, might require both KDM7A and UTX *in vitro*. Indeed, *in vivo*, the inhibition of leukocyte adhesion to the femoral artery in mice was only observed after a treatment with both Daminozide and GSK-J4. These results suggested that a synergism exists between the two histone demethylases, KDM7A and UTX, in inflammatory activated ECs. Although direct evidence of a functional interaction between H3K9me2 and H3K27me3 during the inflammatory response is still lacking, a subset of developmental genes may be cooperatively repressed by both H3K9me2 and H3K27me3 during ESC differentiation (Mozzetta *et al*, 2014; Kurimoto *et al*, 2015).

SEs normally regulate the expression of genes that have especially prominent roles in cell type-specific processes (Pott & Lieb, 2015; Hnisz *et al*, 2017). Although numerous studies have reported the importance of SEs in the maintenance of cell identity and the determination of cell lineage, the significance of *de novo* SE formation during inflammatory responses has also been reported in LPS-stimulated mouse macrophages and TNF- α -stimulated human adipocytes (Hah *et al*, 2015; Schmidt *et al*, 2015). In human ECs, *de novo* SEs are rapidly formed as a mechanism by which a master transcription factor could connect a rapid transcriptional response that drives dynamic change following proinflammatory activation. NF- κ B engaged most endothelial enhancers in response to TNF- α stimuli, and directed BRD4 recruitment to form *de novo* SEs and activated the transcription of many canonical proinflammatory genes (Brown *et al*, 2014b). Our present findings show that the recruitment of KDM7A and UTX was coincident with NF- κ B binding and H3K27ac marks in TNF- α -stimulated human ECs. We defined the SEs by using the ChIP-Seq data for BRD4 and demonstrated that the binding of KDM7A and UTX was dramatically increased at BRD4-SEs, as compared to typical enhancers. In addition, we observed that the KDM7A recruitment preceded the NF- κ B binding to the genome. Thus, KDM7A and UTX might play important roles for the formation of *de novo* SEs in human ECs, although loss-of-function experiments will be required to address this point.

A recent study described the potential mechanisms by which the repressive histone mark H3K27me3 controls the formation of SEs. SEs identified in hair follicle stem cells and their differentiated progeny were either repressed or activated in a lineage-dependent manner. SEs and their surrounding genomic regions associated with genes critical for determining stem cell fate were actively repressed by gaining H3K27me3 marks, in a process termed “super-silencing” during hair follicle stem cell differentiation. Conversely, differentiated progeny fate determinants became de-repressed (activated) by losing H3K27me3 marks to expose new SEs (Adam *et al*, 2015). Here, in human ECs, we have shown that KDM7A and UTX rapidly

mobilized to newly formed SEs where the repressive histone marks H3K9me2 and H3K27me3 were decreased 1 h following the TNF- α stimulus, and were associated with the active transcription of many proinflammatory genes. In contrast, KDM7A and UTX were de-localized from the control-specific SEs (TNF- α -lost SEs) in response to TNF- α , despite the persistent hypomethylation of H3K9me2 and H3K27me3. Thus, these findings provide evidence that repressive histone marks might play important roles for both SE formation and SE loss during the early inflammatory responses in completely differentiated cells.

3C-based technologies have revealed that megabase size TADs are already formed in ES cells and remain relatively constant throughout development (Dixon *et al*, 2012, 2015). However, chromosome reorganization is observed during cellular differentiation at sub-TAD levels (*i.e.*, within megabase size TADs), and these lineage-specific sub-TADs are associated with cell type-specific gene expression programs (Phillips-Cremins *et al*, 2013). However, only few studies have investigated the plasticity of chromosome organization or chromosomal loop formation in response to external stimuli. For example, using Hi-C and 3C methods, a report has confirmed that promoter–enhancer loops pre-exist and are relatively stable during TNF- α signaling in human ECs (Jin *et al*, 2013). In this study, we performed *in situ* Hi-C in combination with active RNA pol II ChIA-PET and found that the megabase size TADs are highly similar between untreated and TNF- α -treated human ECs. However, to our surprise, SE-SE interactions are newly formed at sub-TAD levels at typical TNF- α -responsive inflammatory gene loci, 1 h after TNF- α stimulation. More recently, circadian gene expression was shown to control rhythmic chromatin interactions between enhancers and promoters within sub-TADs, by *in situ* Hi-C in mouse livers harvested 12 h apart (Kim *et al*, 2018). In addition, promoter-anchored chromatin loops were rapidly reorganized within 4 h after inducing the differentiation of 3T3-L1 preadipocytes, as detected using promoter capture Hi-C (Siersbaek *et al*, 2017). Based on these findings, we believe that chromosomal conformation changes, such as SE-SE loops and enhancer–promoter loops, could be rapidly reorganized at sub-TADs levels even in completely differentiated cells in response to external stimuli, including pro-differentiation and inflammatory signals.

In summary, our study offers a new perspective on the spatial transcriptional control during inflammatory responses and delineates the multiple mechanisms utilized by KDM7A and UTX in the regulation of the TNF- α -responsive gene expression program in human ECs (Fig 7). Our findings support a model through which KDM7A and UTX mediate the vast majority of the NF- κ B signaling pathway, likely via the demethylation of repressive histone marks. The evidence showing that the recruitment of KDM7A and UTX to the inflammatory loci following TNF- α -stimuli is associated with the looping between SEs suggests the possible roles of chromatin interactions in early inflammation. Moreover, we demonstrated that the pharmacological and simultaneous inhibition of KDM7A and UTX markedly reduced leukocyte adhesion *in vivo*. A phase III clinical trial (BETonMACE) is in progress to test the effects of RVX 208, a novel, orally active BET protein inhibitor, in patients with an increased risk of cardiovascular disease (Ghosh *et al*, 2017). Clearly, histone modification enzymes are ubiquitously expressed in the human body, and therefore, cell- or tissue-specific targeting might be required for their translational relevance. Nevertheless, KDM7A

and UTX could be novel therapeutic targets for vascular inflammatory diseases, including atherosclerosis.

Materials and Methods

Mice

All mouse experiments were approved by The University of Tokyo Animal Care and Use Committee (approval number; H29-1). Male C57BL/6N mice aged 10 weeks were purchased from Japan SLC (Shizuoka, Japan). The animals were housed in individual cages in a temperature- and light-controlled environment and had *ad libitum* access to chow and water.

Cell lines

Human umbilical vein endothelial cells (HUVECs) were used as human ECs in this work. HUVECs were purchased from Lonza Japan Ltd. (Tokyo, Japan) and cultured and passaged every 2 or 3 days in EBM-2 complete medium composed of EBM-2 Basal Medium (Lonza), supplemented with EGM-2 SingleQuot Kit Suppl. & Growth Factors (Lonza) and 3% fetal bovine serum (FBS) (Thermo Fisher Scientific, Waltham, MA). We sub-cultured HUVECs when they reached 80–90% confluence, to avoid excessive floaters. HUVECs were used within passages 4–7 for all experiments in this work. The human monocyte cell line U937 was purchased from the JCRB Cell Bank (Osaka, Japan) and grown and passaged every 2 or 3 days in RPMI1640 (Thermo Fisher Scientific), supplemented with 1% penicillin/streptomycin (Wako, Osaka, Japan) and 10% FBS. All cells were cultured at 37°C and in a 5% CO₂ atmosphere in a humidified incubator.

TNF α stimulation

HUVEC plates (80–90% confluent) were washed with PBS once and then serum starved in EBM-2 Basal Medium containing 0.5% FBS for 16 h. HUVECs were stimulated with or without 10 ng/ml TNF- α (Peprotech, Rocky Hill, NJ) for the indicated periods thereafter.

mRNA and miRNA isolation

Total RNA, including miRNA, was isolated from HUVECs using a miRNeasy Micro Kit (Qiagen, Hilden, Germany) with the DNase digestion step, according to the manufacturer's instructions.

miRNA microarray

The miRNA microarray (Human miRNA Microarray, Release 19.0, 8x60K; Agilent Technologies, Santa Clara, CA) was carried out by MBL (Aichi, Japan).

Transfection procedure

Synthetic miRNA mimics for miR-374b-5p, miR-374a-5p, and miR-3679-5p, negative control miRNA mimics, as well as inhibitors for miR-3679-5p and negative control inhibitors were obtained from Thermo Fisher Scientific. siRNAs for lysine demethylase 7A

(KDM7A) and 6A (UTX), and negative control siRNA were purchased from Thermo Fisher Scientific or Sigma-Aldrich (St. Louis, MO). Sequences of miRNA mimics and siRNAs are listed in Appendix Table S1. miRNA mimics, miRNA inhibitors, or siRNAs were transfected with Lipofectamine[®] RNAiMAX reagent (Thermo Fisher Scientific) according to the manufacturer's protocol. Growth medium was replaced 5 h after transfection.

Real-time PCR for mRNA quantification

The isolated RNA (500 ng) was reverse-transcribed to cDNA with PrimeScript RT Master Mix (Takara, Shiga, Japan). PCR was performed with a CFX96 unit (Bio-Rad, Hercules, CA) with SYBR[®] Premix EX Taq[™]II (Takara). Relative expression levels were calculated using β -actin (ACTB) mRNA as a reference. The primers for quantification are listed in Appendix Table S1.

Western blot

Whole cells were lysed in M-PER[®] Mammalian Protein Extraction Reagent (Thermo Fisher Scientific), and then, the lysate was centrifuged at 10,000 \times g for 10 min to pellet the cell debris. The supernatant was mixed with 5 \times Lane Marker Sample Buffer (Thermo Fisher Scientific) and then incubated for 5 min at 95°C. Proteins were separated by SDS-PAGE and then transferred to nitrocellulose membranes (Bio-Rad). After blocking with 4% BLOCK ACE blocking agent (DS Pharma Biomedical, Osaka, Japan), the membrane was incubated with the following antibodies: monoclonal rabbit anti-vascular cell adhesion molecule-1 (VCAM1) (1:2,500 dilution) (Abcam, Cambridge, MA), polyclonal rabbit anti-intracellular cell adhesion molecule-1 (ICAM1) (1:2,500 dilution) (Cell Signaling Technology, Danvers, MA), polyclonal rabbit-E-selectin (SELE) (1:1,000 dilution) (Santa Cruz Biotechnology Inc., Santa Cruz, CA), and mouse monoclonal anti-ACTB (1:5,000) (Sigma-Aldrich) at 4°C overnight. The blots were then incubated with a peroxidase-conjugated anti-rabbit or mouse IgG antibody (1:10,000 dilution) (Bio-Rad) at 37°C for 40 min. The antibody-antigen reaction was detected with the Clarity[™] Western ECL Substrate (Bio-Rad).

Adhesion assay

Monocyte adhesion to HUVECs was assayed as previously described (Inoue *et al*, 2006; Tozawa *et al*, 2011). In brief, HUVECs were grown to confluence in a 24-well cell culture plate. U937 cells were labeled with the fluorescent dye Calcein AM (Thermo Fisher Scientific) in EBM2 containing 0.5% FBS. HUVECs transfected with miRNA mimics or siRNAs were incubated with or without TNF- α (10 ng/ml) for 4 h, and then, U937 cells were added to the plate in a final concentration of 3×10^5 cells per well. After 1 h, the cells were washed twice with Hanks' balanced salt solution containing calcium and magnesium (Thermo Fisher Scientific). Adhesion of U937 cells was visualized with a fluorescent microscope. Nine microscopic fields under each condition were photographed at random, using a Leica DMI6000 B camera with an Adaptive Focus Control system (Leica Microsystems K.K. Tokyo, Japan), and then, the U937 cells were automatically counted with the ImageJ 1.48v program (<https://imagej.nih.gov/ij/download.html>).

RIP followed by microarray

RNA immunoprecipitation (RIP) was performed using a RiboCluster Profiler RIP assay kit for microRNA (#RN1005; MBL), according to the manufacturer's protocol. Briefly, HUVECs transfected with miR-3679-5p or negative control miRNA mimics were stimulated with TNF- α and then immunoprecipitated with magnetic Dynabeads M-280 (Thermo Fisher Scientific) coupled with an anti-EIF2C2/AGO2 mouse monoclonal antibody (MBL). A mouse IgG2a Isotype control antibody (MBL) was used as a negative control to confirm the proper functioning of the RIP assay (data not shown). Large RNAs and small RNAs were separately extracted from the antibody immobilized beads-RNP complex, and then, the AGO2-bound large RNAs were subjected to the microarray analysis.

Preparation of cRNA and hybridization of probe arrays were performed according to the manufacturer's instructions (Affymetrix, Santa Clara, CA, USA). Affymetrix Genechip Human Genome U133 plus 2.0 arrays containing over 54,000 probe sets were used. The expression value for each mRNA was obtained with the Affymetrix Microarray Suite 5 method (MAS5). To analyze the expression data at the genetic level, the probes with the highest expression value for each gene were selected, and subsequently, the probes exhibiting a value of more than 1,000.0 in at least one condition were screened. Finally, probes with an average fold change (miR-3679-5p/control) > 2.0 or < 0.5 were extracted.

Luciferase assay

The 3'-UTRs of the human KDM7A and UTX mRNAs were amplified by PCR from the cDNA of HUVECs and cloned at the *Sac1-Xba1* sites for KDM7A and the *Sac1-Xho1* sites for UTX into the pmirGLO Dual-Luciferase miRNA Target Expression Vector (Promega, Madison, WI). The PCR primers and oligonucleotide sequences for the constructs are listed in Appendix Table S1. All of the constructs were further confirmed by sequencing. For the luciferase activity analysis, each construct was co-transfected with the miRNA mimics in a 12-well plate, using the DharmFECT Duo transfection reagent (Horizon Discovery, Cambridge, UK) for 24 h, and the luciferase assays were performed with the Dual-Glo Luciferase assay system (Promega), according to the manufacturer's protocol. The transfection efficiency for each well was normalized by the Renilla luciferase activity.

Cloning of KDM7A and UTX

Human full-length KDM7A was produced by ligating the fragment of 1–382 bp obtained by synthesis (Thermo Fisher Scientific) and the 382–2,816 bp fragment cloned by PCR using cDNA from HUVECs. UTX was cloned by PCR using cDNA from the pluripotent human testicular embryonal carcinoma cell line, NTERA-2 cl.D1 (American Type Culture Collection, Manassas, VA). The PCR primers and oligonucleotide sequences for the constructs are listed in Appendix Table S1. The cDNA was subcloned into pIRES2-EGFP (Clontech, Shiga, Japan) and then transferred into the pShuttle2 and pAdeno-X Viral DNA (Clontech) by using the Adeno-X adenoviral expression system1 (Clontech). All cloned constructs were confirmed by restriction enzyme digestions and DNA sequencing.

Adenovirus infection

We preliminarily performed a setup experiment to test different multiplicities of infection (MOI), and an MOI of 100 was considered to be optimum (data not shown). Therefore, we applied an MOI of 100 for further analysis in this study. One day before the transduction, 1.0×10^6 HUVECs were seeded into 15-cm dishes in 15 ml of EBM-2 complete medium. The HUVECs exhibited 80–90% confluence at the time of transduction. Adenovirus particles were mixed with 2 ml of Opti-MEM™ Reduced Serum Medium (Thermo Fisher Scientific) and incubated for 30 min at room temperature. HUVECS were washed with PBS once and then incubated with 2 ml of the adenovirus containing Opti-MEM™ Reduced Serum Medium for 1 h at 37°C in a 5% CO₂ atmosphere in a humidified incubator. Afterward, 15 ml of EBM-2 complete medium was added to the culture dish.

Intravital microscopy

Male, 10-week-old C57BL/6N mice ($n = 3\text{--}4$ /group) were pretreated with vehicle (5% DMSO), Daminozide (50 mg/kg), GSKJ4 (50 mg/kg), or mixed inhibitor (Daminozide+GSKJ4, 50 mg/kg each) at 16 h and 1 h prior to TNF- α treatment. Inflammation was induced by an intraperitoneal injection of mouse recombinant TNF- α (Pepro-Tech) at a dose of 5 μ g/mouse. Leukocyte adhesive interactions in the femoral arteries were assessed by intravital microscopy (IVM), as previously described (Osaka *et al*, 2007; Ito *et al*, 2016). In brief, mice were injected with rhodamine 6G chloride (Molecular Probes, Eugene, OR) via the right femoral vein to label leukocytes *in vivo*. The left femoral artery was visualized with a microscope (model BX51WI; Olympus, Tokyo, Japan) equipped with a water immersion objective. Labeled leukocytes were clearly visualized in the anterior half of the vessels facing the objective, and platelets < 5 μ m in diameter were excluded. All images were recorded using a personal computer with an image analysis program (MetaMorph; Molecular Devices, Sunnyvale, CA). The numbers of adherent and rolling leukocytes (*i.e.*, those that did not move for ≥ 3 s during the 1-min recording period and those that passed a reference line perpendicular to the vessel axis, respectively) were counted along a region of interest, a $100 \times 100 \mu$ m segment of the vessel, and expressed as the number of interacting cells per $10^4 \mu$ m² of the vessel surface.

ChIP

Chromatin immunoprecipitation (ChIP) was performed as previously described (Kanki *et al*, 2011, 2017). In brief, 10 million HUVECs were cross-linked with 1% formaldehyde (Wako) for 10 min. For the p65 and FLAG ChIP analyses, cells were fixed with 2 mM EGS (ethylene glycol bis [succinimidyl succinate]) (Thermo Fisher Scientific) for 1 h prior to formaldehyde fixation. After neutralization by using 0.2 M glycine, the cells were collected, resuspended in 2 ml SDS lysis buffer, composed of 10 mM Tris-HCl, pH 8.0 (Thermo Fisher Scientific), 150 mM NaCl (Thermo Fisher Scientific), 1% SDS (Sigma-Aldrich), 1 mM EDTA, pH 8.0 (Thermo Fisher Scientific), and cComplete™ EDTA-free Protease Inhibitor Cocktail (Sigma-Aldrich), and fragmented by a Picoruptor (40 cycles for histones and p65, and 20 cycles for FLAG, 30 sec on/30 sec off; Diagenode, Liege Science Park, Belgium). The sonicated

solution was diluted with ChIP dilution buffer [20 mM Tris-HCl, pH 8.0, 150 mM NaCl, 1 mM EDTA, 1% Triton X-100 (Sigma-Aldrich)] up to 10.3 ml, and 10 ml was used for immunoprecipitation (10 ml) and the remaining 300 μ l was saved as non-immunoprecipitated chromatin (INPUT). The specific antibody was bound to magnetic Dynabeads M-280 and applied to the diluted, sonicated solution for immunoprecipitation. Antibodies against H3K4me3, H3K27ac, H3K9me2, H3K27me3 (MAB Institute, Inc. Hokkaido, Japan), p65 (Abcam for ChIP-Seq and Santa Cruz Biotechnology Inc. for ChIP-PCR), and FLAG (Sigma-Aldrich) were used. The prepared DNA was quantified using a NanoDrop 2000 spectrophotometer (Thermo Fisher Scientific), and more than 10 ng of DNA was processed for qPCR or sequencing.

ChIP-qPCR

The primers for quantification are listed in Appendix Table S1. PCR was performed with a CFX96 PCR and SYBR[®] Premix EX Taq[™]II. Fold enrichment was determined as the percentage of the input.

ChIP-seq library preparation

For the ChIP-seq analysis using the FLAG antibody, the precipitated DNA from the original DNA size of ~2 kb was further sheared to ~200 bp by an Acoustic Solubilizer (Covaris, Woburn, MA). For ChIP-seq using an antibody against histones, DNA sonicated to an average size of 0.5 kb was used for the ChIP-seq library preparation. ChIP samples were processed for library preparation with a KAPA Hyper Prep Kit (Kapa Biosystems Inc., Wilmington, MA), according to the manufacturer's instructions. Deep sequencing was performed on a HiSeq 2500 sequencer (Illumina Inc., San Diego, CA) as single-end 50 base reads.

RNA-seq library preparation

Total RNA from the cells was isolated as described above. The RNA integrity score was calculated with the RNA 6000 Nano reagent (Agilent Technologies) in a 2100 Bioanalyzer (Agilent Technologies). All samples used for the preparation of the RNA-seq libraries had a RIN (RNA Integrity Value) score above 9. RNA-seq libraries were prepared with a TruSeq RNA Library Prep Kit (Illumina). The libraries were sequenced on a HiSeq 2500 system (Illumina) as paired-end 150 base reads.

ChIA-PET library preparation

Chromatin interaction analysis with paired-end tag sequencing (ChIA-PET) was performed as previously described (Li *et al*, 2010; Papantonis *et al*, 2012). Briefly, cells were cross-linked using 10 mM EGS in 50% glacial acetic acid (45 min) and then in 1% paraformaldehyde (20 min), quenched (5 min) in 2.5 M glycine, harvested, and sonicated (Digital Sonifier 250; Branson, Danbury, CT). The ChIP was performed using magnetic beads (Dynabeads M-280) with the Pd75C9 antibody directed against phospho-Ser2-/Ser5 within the heptad repeat at the C-terminus of the largest catalytic subunit of RNA polymerase II (a gift from H. Kimura). The chromatin captured on the magnetic beads was trimmed to create blunt ends, phosphate groups were added to the 5' ends, the ends were

ligated to each other via biotinylated half-linkers, and the complexes were eluted. After the crosslinking was reversed, the DNA was purified and digested with *Mme*I (binding site encoded by the linker). After immobilization on M-280 Streptavidin Dynabeads (Thermo Fisher Scientific), the adaptors were ligated, and the efficiency of library production was evaluated by PCR. Finally, the di-tags were prepared, the library was sequenced on a GAII analyzer (Illumina), and the resulting paired-end tags (PETs) were analyzed.

In situ Hi-C library preparation

In situ Hi-C was performed in two replicates for HUVECs treated with or without TNF- α for 60 min. Cells were cross-linked for 10 min at room temperature with 1% formaldehyde and quenched for 5 min at room temperature with 0.2 M glycine. The cross-linked cells were centrifuged at 2,500 \times g for 5 min at 4°C. To isolate nuclei, cross-linked cells were resuspended in 200 μ l of lysis buffer [10 mM Tris-HCl (pH 8.0), 10 mM NaCl, 0.2% NP-40, Protease Inhibitor Cocktail (Sigma-Aldrich)] and incubated on ice for 15 min. The suspension was then centrifuged at 2,500 \times g for 5 min, and the pellet was washed by resuspension in 300 μ l of lysis buffer and centrifugation at 2,500 \times g for 5 min at 4°C. The pellet was resuspended in 50 μ l of 0.5% SDS and incubated for 10 min at 62°C. After heating, 170 μ l of 1.47% Triton X-100 was added to the suspension and incubated for 15 min at 37°C. To digest the chromatin, 25 μ l of 10 \times NEBuffer2 and 100 U *Mbo*I (New England Biolabs, Beverly, MA) was added to the suspension and incubated at 37°C overnight with rotation. Enzymes were inactivated by heating for 20 min at 62°C. Fragmented ends were biotin-labeled by adding 50 μ l of a mixture containing 0.3 mM biotin-14-dATP (Thermo Fisher Scientific), 0.3 mM dATP (Thermo Fisher Scientific), 0.3 mM dTTP (Thermo Fisher), 0.3 mM dGTP (Thermo Fisher Scientific), and 0.8 U/ μ l Klenow (Enzymatics, Beverly, MA) and incubating the solution for 1 h at room temperature with rotation. The biotin-labeled fragmented ends were subsequently ligated by adding 900 μ l of a mixture containing 120 μ l of 10 \times T4 DNA ligase buffer (New England Biolabs), 100 μ l of 10% Triton X-100, 12 μ l of 10 mg/ml BSA (New England Biolabs), 5 μ l of 400 U/ μ l of T4 DNA Ligase (New England Biolabs), and 663 μ l H₂O, and incubating the solution for 4 h at room temperature with rotation. The nuclei were pelleted for 5 min at room temperature at 2,500 \times g. After removing the supernatant, the nuclei were resuspended in 550 μ l of 10 mM Tris-HCl (pH 8.0). The nuclei were reverse-cross-linked by adding 50 μ l of Proteinase K (New England Biolabs) and 57 μ l of 10% SDS, and incubating the mixture for 30 min at 55°C. Subsequently, the nuclei were mixed with 67 μ l of 5 M NaCl and incubated at 68°C overnight. After cooling the samples for 10 min at room temperature, the DNA was captured with 0.8 \times AMPureXP beads (Beckman Coulter Inc., Brea, CA) and eluted in 100 μ l of 10 mM Tris-HCl (pH 8.0). DNA shearing was performed using a focused-ultrasonicator (Covaris, E220; Power 140 W, Duty factor 10%, Cycle per burst 200, Time 67 s, temperature 7°C), and the final sample volume after shearing was brought to 200 μ l with 10 mM Tris-HCl (pH 8.0). To design the DNA selection for 200–600 bp size, a 120 μ l aliquot of AMPureXP beads was added to 200 μ l of sample (beads ratio: 0.6) and incubated for 5 min at room temperature with inversion. To remove the DNA fragments > 600 bp, the clear supernatant was collected on a magnet and the beads were discarded. As a second

round of size selection, an 80 μ l aliquot of AMPureXP beads was added to the supernatant and incubated for 5 min at room temperature with inversion. The supernatant was removed on a magnet, and the beads were washed twice with 700 μ l of 70% ethanol and dried for 5 min. DNA fragments (200–600 bp) were eluted from the beads with 300 μ l of 10 mM Tris–HCl (pH 8.0). For the biotin pull down, a 100 μ l aliquot of 10 mg/ml Dynabeads My One T1 Streptavidin beads (Thermo Fisher Scientific) was washed with 1 \times Tween Wash Buffer (5 mM Tris–HCl (pH 7.5), 0.5 mM EDTA, 1 M NaCl, 0.05% Tween). The beads were resuspended in 300 μ l of 2 \times Binding Buffer [10 mM Tris–HCl (pH 7.5), 1 mM EDTA, 2M NaCl], transferred to sample tubes, and incubated for 15 min at room temperature. The beads were subsequently washed twice with 1 \times Tween Wash Buffer for 2 min at 55°C with mixing and washed once with 1 \times NEB T4 DNA ligase buffer (Enzymatics). To repair the fragmented ends and remove the biotin from unligated ends, the beads were resuspended in 85 μ l of 1 \times NEB T4 DNA ligase buffer (Enzymatics), 5 μ l of 10 mM dNTP Mix (Thermo Fisher Scientific), 5 μ l of 10 U/ μ l NEB T4 PNK (New England Biolabs), 4 μ l of 3 U/ μ l NEB T4 DNA Polymerase (New England Biolabs), and 1 μ l of 5 U/ μ l Klenow (Enzymatics), and incubated for 30 min at room temperature. After the supernatant was discarded on a magnet, the beads were washed twice with 1 \times Tween Wash Buffer for 2 min at 55°C with mixing and resuspended in 100 μ l of 1 \times NEB Buffer2. For dA-tailing, the beads were resuspended in 90 μ l of 1 \times NEB Buffer2, 5 μ l of 10 mM dATP (Thermo Fisher Scientific), and 5 μ l of 5 U/ μ l Klenow (3'→5' exo-) (Enzymatics), and incubated for 30 min at 37°C. The beads were subsequently washed twice with 1 \times Tween Wash Buffer as before and once with 1 \times NEB Quick Ligation Reaction Buffer (New England Biolabs). To ligate the adapters, the beads were resuspended in 50 μ l of 1 \times NEB DNA Quick Ligation Reaction Buffer, 1 μ l of NEXTflex[®] DNA Barcodes (Bioo Scientific, Austin, TX), and 2 μ l of NEB DNA Quick Ligase (New England Biolabs), and incubated for 15 min at room temperature. The beads were washed twice with 1 \times Tween Wash Buffer as before and once with 10 mM Tris–HCl (pH 8.0) and resuspended in 20 μ l of 10 mM Tris–HCl (pH 8.0). After estimating the concentration and the cycle number for the final PCR by a qPCR assay, the final PCR was directly performed with the T1 beads, using a KAPA Hyper Prep Kit (KAPA Biosystems Inc.). The DNA was cleaned with 1 \times AMPure beads, eluted in 30 μ l of 10 mM Tris–HCl (pH 8.0), and analyzed by paired-end sequencing.

Bioinformatics

RNA-seq data analysis

Sequence reads (150-bp paired read) were aligned to the human reference genome (GRCh37/hg19) with Tophat (version: 2.1.1) (Kim *et al*, 2013) with the following parameters: The mismatch to the reference genome should be supported by at least 2 reads, and the lengths of insertions and deletions should be supported by at least 3 bp. After assigning the mapped reads onto the gene positions deposited in the geocode database (https://www.genencodegenes.org/mouse/release_M19.html), the FPKMs (fragments per kilobase of exon per million reads) of all of the deposited genes were calculated by Cufflinks (Trapnell *et al*, 2010) with the default parameters. RNA-seq signals were visualized with the Integrative Genomics Viewer (Version 2.4.8) (<http://software.broadinstitute.org/softwa>

re/igv/). The RNA-seq signal of each locus was normalized by the following basis:

$$\text{Signal on each locus} = \frac{\text{Number of mapped reads on each locus} \times 1,000,000}{\text{Total number of mapped reads}}$$

Reproducibility between RNA-seq experiments

The reproducibility of the genome-wide RNA-seq signals in the biological replicates was examined under all conditions. The FPKM values were used as the RNA-seq signals. Subsequently, the correlation coefficients between two biological replicates were calculated, based on the FPKMs of each reference gene.

Gene ontology analysis

The gene annotation enrichment analysis was performed for the Gene Ontology (biological process and cellular component), using the Functional Annotation tool at DAVID Bioinformatics Resources 6.7 (<http://david.abcc.ncifcrf.gov/>).

PCA analysis

The first three eigenvectors of the six samples (*i.e.*, control, TNF- α , TNF- α with BAY 11-7082, siKDM7A, siUTX, and siKDM7A+siUTX) were used to analyze the expression patterns of TNF- α -responsive genes. In total, 404 TNF- α -up-regulated genes (more than 2-fold after TNF- α treatment in comparison with the control) and 136 TNF- α -down-regulated genes (< 0.5-fold after TNF- α treatment in comparison with the control) were used as the TNF- α -responsive genes in the principal component analysis (PCA). The variances of each eigenvector are 74.9% for PC1, 9.6% for PC2, and 6.4% for PC3, respectively.

ChIP-Seq data analysis

The quality of FASTQ files was evaluated using FastQC (<http://www.bioinformatics.babraham.ac.uk/projects/fastqc>) version 0.11.8. TruSeq adaptor sequences, and low-quality base calls were trimmed using Trimmomatic SE version 0.39 with “ILLUMINACLIP: adaptor_sequence.fa:2:30:7 LEADING:3 TRAILING:3 SLIDING-WINDOW:4:15 MINLEN:36” options. The trimmed reads were aligned to the hg19 human reference genome using Bowtie2 version 2.3.4.3 with a “-N 1” option. SAM files were sorted and converted into BAM files using Samtools version 1.9. Duplicated and low-quality (MAPQ < 10) reads were removed using Picard (<http://broadinstitute.github.io/picard/>) version 2.19.0 and Samtools. To visualize the sequencing tracks, BIGWIG files were generated from BAM files using deepTools version 3.3.0 bamCoverage with “-of bigwig -bs 1 -exactScaling -normalizeUsing CPM -e 2000” (H3K9me2, H3K27me3, and their input controls), or “-of bigwig -bs 1 -exactScaling -normalizeUsing CPM -e 300” options. The BIGWIG files were displayed using the Integrative Genomics Viewer. The putative binding sites (peaks) of KDM7A and UTX were analyzed by SICER (version: 1.1) with the default parameter settings (Window size: 200 bp, Gap size: 400 bp, E-value: 100). The putative binding sites (peaks) of p65 were analyzed by MACS (version 1.4.2) (Zhang *et al*, 2008) with the default parameter settings.

Reproducibility between ChIP-seq experiments

The reproducibility of the genome-wide ChIP-seq signals for KDM7A and UTX was examined by comparing two biological replicates. The normalized read counts in every 10,000-bp genomic region were computed using deepTools multiBigwigSummary with “-outRawCounts -bs 10000 -n 0” options.

Distribution of ChIP-seq signals

The ChIP-seq signals of H3K27ac, p65, KDM7A, and UTX in human ECs with or without TNF- α treatment were compared in the TNF-specific binding sites of KDM7A or UTX. In each binding site, the 10-kb regions from the centers of the KDM7A and UTX binding sites were screened, and the ChIP-seq signals were normalized by the total read counts.

Genomic regions enrichment of annotations tool (GREAT)

GREAT version 3.0.0 (<http://great.stanford.edu/public/html/index.php>) was performed on the KDM7A and UTX binding regions obtained from the ChIP-seq results, in order to identify their functional annotations (McLean *et al*, 2010).

De novo motif analysis

The *de novo* binding motifs were identified by the MODIC motif identification program (window size: 12 bp, background sequence: random genomes, enrichment ratio: > 2.0-fold change compared to random genomes) (Nakaki *et al*, 2012). The ten sequence motifs enriched in each ChIP-seq assay were outputted by the program and integrated into three motifs, based on the sequence patterns. Specifically, the sequence pattern of each motif was converted into a position weight matrix, and the motifs with correlation coefficients > 0.8 between two matrices were integrated to the significant one. The three *de novo* motifs were assigned to the known TF-binding motifs deposited in TRANSFAC (Matys *et al*, 2003) (<http://genexplain.com/transfac/>) by using the STAMP web tool (Mahony & Benos, 2007) (<http://www.benoslab.pitt.edu/stamp/>).

Boxplot

The p65 binding sites before and after TNF- α stimulation were merged as the set of the total p65 binding sites. The set includes three patterns (*i.e.*, control-specific, common, and TNF- α -specific) of p65 binding. The normalized read counts for each site of the set were calculated for the ChIP-seq analyses of p65, H3K27ac, KDM7A, and UTX before and after TNF- α stimulation. To determine whether a significant difference exists between binding before and after TNF- α stimulation, the Student's t-test was used to compare the binding distributions of both treatments after normalization. The normalized read counts were calculated as follows:

$$\text{Signal on each p65 binding site (Normalized read count)} = \frac{\text{Number of mapped on reads each binding site} \times 20,000,000}{\text{Size of each binding site} \times \text{Total number of mapped reads}}$$

Prediction of super enhancers in TNF-treated conditions

Super enhancers (SEs) were predicted using the ROSE software package, as described in (Loven *et al*, 2013; Whyte *et al*, 2013) and available at (younglab.wi.mit.edu/super_enhancer_code.html). First, the BRD4 ChIP-seq data were downloaded from GSE54000 (<https://www.ncbi.nlm.nih.gov/geo/query/acc.cgi?acc=GSE54000>), and the binding sites were analyzed as described in the section “ChIP-seq data analysis”. Subsequently, super enhancers were identified by ROSE. The putative super enhancers were ranked, based on the BRD4-binding intensities and the special enrichment of BRD4-binding sites. Comparing the BRD4-binding sites in HUVECs with or without TNF- α treatment, the super enhancers were classified into three groups: TNF- α -specific, control-specific, and common. The sites with more than 1-bp overlapping between TNF- α 0 and 60 min are regarded as “common” super enhancers.

Scatter plot

To visualize the effects of TNF- α stimulation on the gene recruitments by KDM7A (Fig 3A) and UTX (Fig 3B), the log₂ fold changes of mRNA-seq expression levels (horizontal axis) and KDM7A and UTX ChIP-seq binding levels (vertical axis) between TNF- α -stimulated and non-TNF- α -stimulated samples were plotted. The genes were categorized by the log₂ fold changes as the TNF- α -up-regulated genes (red; FC > 1.5), TNF- α -down-regulated (blue; FC < 1.5), and unchanged (gray; other).

NGS plot

To compare the effects of TNF- α stimulation on the recruitment of KDM7A and UTX, the average ChIP-seq expression levels of KDM7A (Fig 3C) and UTX (Fig 3D) around the transcription start sites (TSS) of target genes were plotted using an NGS plot (Shen *et al*, 2014), where the target genes were selected as the TNF- α -up-regulated and TNF- α -down-regulated genes (up: FC > 4, down: FC < 2).

The effects of TNF- α stimulation on the recruitments between the SEs and typical enhancers (TEs) were compared for KDM7A (Fig 5D) and UTX (Fig 5E) via a comparison of the ChIP-seq expression levels after the TNF- α stimulations around the SE and TE regions, using an NGS plot. The SEs in Fig 5D and E included all of the control-specific, common, and TNF- α -specific SEs as defined above. TEs were downloaded from the pre-compiled HUVECs *ngsplotdb* (*ngsplotdb_hg19_75_3.00_enhancer.tar.gz*) (<https://github.com/shenlab-sinai/ngsplot>).

Analyses of repressive histone modification scores

The enrichment of ChIP-seq reads (H3K9me₂, H3K27me₃, and their input DNAs) in gene bodies with TNF- α treatment (TNF⁺) and control (TNF⁻) was quantified in Reads Per Kilobase Million (RPKM). The log₂ fold change of ChIP enrichment, compared with its input DNA, was then computed for each of the KDM7A- and UTX-target genes and shown by box plots (Fig 4A and B). The KDM7A- and UTX-target genes were selected as follows: (i) The log₂ fold change of mRNA-seq expression levels with TNF- α treatment (TNF⁺) and control (TNF⁻) was larger or equal to 2; (ii) the

log₂ fold change of ChIP signal between a ChIP experiment (KDM7A or UTX) and its input DNA was larger or equal to 0.5.

ChIA-PET data processing

Base data processing of ChIA-PET data was performed as previously described. Briefly, ChIA-PET libraries yielded $\sim 35 \times 10^6$ 20-bp paired-end reads each, from which 10.8×10^6 and 8.8×10^6 were successfully aligned to the genome (hg19) for the 0-, 30-, and 60-min samples, respectively. For stringency, two or more reads with the same sequences, or mapping within 2 bp of the left and right ends of another read, were classified as one PET.

Analysis of ChIA-PET interaction changes

The range of each binding site was set to 10 kb. The number of ChIA interactions that started on each binding site was normalized, using the total ChIA count for each condition. For each binding site, the rate of the interaction count was plotted as Bean plots or Pirate plots.

Hi-C data processing

The numbers of Hi-C paired reads for control replicate 1, 2 and TNF- α -treated replicate 1, 2 were 174,690,226, 185,378,925, 186,095,480, and 175,580,289, respectively. All 4 Hi-C data were processed separately by Hi-C pro 2.9.0 (Servant *et al*, 2015) using GRCh37/hg19 human genome sequence derived at UCSC web site. We exclude duplicated pairs and also excluded self, dangling end, re-ligation, single, and dumped pairs using the fragment information for MboI restriction enzyme (default option of Hi-C pro). The valid interactions named as “allValidPairs” for 2 control and 2 treated were 97,307,916 (55.7%), 105,692,339 (57.0%), 108,491,410 (58.3%), and 103,012,810 respectively. The replicate Hi-C data for control and treated were merged and converted to “.hic” format using “hicpro2juicebox.sh” program respectively, and 196,814,231 and 204,936,615 valid pairs of reads finally remained for the control and TNF- α -treated samples, respectively. These control and TNF- α -treated Hi-C data were used for further analyses.

Contact matrices

The raw Hi-C data of chromosomes 1 and 4 were exported using Juicer-Tools with 1 Mb, 50 kb, and 3 kb bin sizes. Interaction scores were visualized by a color gradient, as shown in Fig 6A and B.

Virtual 4C

Virtual 4C data show the interaction counts starting at viewpoints (within 5 kb), which are extracted from Hi-C data. Those viewpoint-containing interactions were counted by 10 kb bins to either end position. The count-data is then shown as a line graph. The virtual 4C data of TNF- α were normalized by those of the control (*i.e.*, no TNF- α treatment).

Hi-C loop calling (HiCCUPS)

To search loops of Hi-C matrix, we used HiCCUPS algorithm (Rao *et al*, 2014) using `juicer_tools.1.8.9_jcuda.0.8.jar` with following

parameter “-r 5000,10000,25000 -f .1,.1,.1 -p 4,2,1 -i 7,5,3 -t 0.02,1.5,1.75,2 -d 20000,20000,50000” for control and treated data. The Hi-C raw contact matrix (of 3k, 5k or larger resolution) and the significant loops by hiccups were viewed by juicebox and our in-house programs.

TAD boundary calling

For calculating topologically associating domain (TAD), we used “TADtool” version 0.77 (Kruse *et al*, 2016) and python version 3.6.5. For Hi-C matrix of 10k bps resolution, “TADtool” program was applied with the option window size as 100,000 (=100k bps) and cutoff as 10.

APA score

For each loop, APA score was calculated using matrix data of 5k bps resolution. An APA score was calculated as the equation the interaction count at loop divided by the average count of surrounding “donuts” regions as described previously (Rao *et al*, 2014).

Quantification and statistical analysis

Statistical differences were analyzed by the Tukey–Kramer test for multiple comparisons. Differences between two groups were compared by the Student’s *t*-test. In all tests, differences with *P*-values of < 0.05 were considered statistically significant.

Data and software availability

The array and sequence data can be accessed through the Gene Expression Omnibus (GEO) under the NCBI accession number GSE121522 (<https://www.ncbi.nlm.nih.gov/geo/query/acc.cgi?acc=GSE121522>).

Expanded View for this article is available online.

Acknowledgements

We thank Ai Higashijima for graphic drawing, Mai Hasegawa, Natsuko Nakada, and Mika Kobayashi (The University of Tokyo) for experimental technical support, Naoto Imamachi, Shiro Fukuda, and Shogo Yamamoto (The University of Tokyo) for bioinformatics analysis, respectively. This work was supported by a Grant-in-Aid for JSPS Postdoctoral Fellows (to Y.H.), a Grant-in-Aid for JSPS Overseas Fellows (to Y.A.), a Grant-in-Aid for Young Scientists (B) 17K15991 (to Y.H.), a Grant-in-Aid for Young Scientists (A) 26710013 (to Y.K.), a Grant-in-Aid for Scientific Research (B) [18H02824 (to M.N.) and 17H03614 (to Y.K.)], a Grant-in-Aid for Scientific Research on Innovative Areas (Research in a proposed research area) 25125707 (to Y.K.), a Grant-in-Aid for Challenging Exploratory Research [26670397 (to Y.K.) and 16K15438 (to Y.K.)], a Fund for the Promotion of Joint International Research (Fostering Joint International Research) 15KK0251 (to Y.K.), AMED CREST [18gm0510018h0106 (to S.T.) and 16gm0510005h0006 (to H.K. and Y.W.)], MEXT KAKENHI 18H05527 (to H.K.), a Research grant by Nanken-Kyoten, TMDU (to Y.H., Y.K., Y.W., and T.F.), a Research grant by Takeda Science Foundation (to Y.K.), a Research grant by Japan Heart Foundation (to Y.K.), a Research grant by MSD Life Science Foundation (to Y.K.), and a Research grant by Kowa Life science Foundation (to Y.K.).

Author contributions

YH, CKG, and YK designed the research strategies; YH, YA, MO, AT, MM, XR, GL, TI, and YK performed the experiments; YH, YM, TS, RN, NN, ST, VML, RW, TT, and YK performed the bioinformatic analyses; MY, MN, HK, TF, HA, YW, and YR interpreted the data and reviewed the manuscript; YH, CKG, and YK wrote the manuscript.

Conflict of interest

The authors declare that they have no conflict of interest.

References

- Adam RC, Yang H, Rockowitz S, Larsen SB, Nikolova M, Oristian DS, Polak L, Kadaja M, Asare A, Zheng D *et al* (2015) Pioneer factors govern super-enhancer dynamics in stem cell plasticity and lineage choice. *Nature* 521: 366–370
- Agarwal V, Bell GW, Nam JW, Bartel DP (2015) Predicting effective microRNA target sites in mammalian mRNAs. *Elife* 4: e05005
- Agger K, Cloos PA, Christensen J, Pasini D, Rose S, Rappsilber J, Issaeva I, Canaani E, Salcini AE, Helin K (2007) UTX and JMJD3 are histone H3K27 demethylases involved in HOX gene regulation and development. *Nature* 449: 731–734
- Bailey P, Chang DK, Nones K, Johns AL, Patch AM, Gingras MC, Miller DK, Christ AN, Bruxner TJ, Quinn MC *et al* (2016) Genomic analyses identify molecular subtypes of pancreatic cancer. *Nature* 531: 47–52
- Bartel DP (2018) Metazoan microRNAs. *Cell* 173: 20–51
- Benjamin EJ, Blaha MJ, Chiuve SE, Cushman M, Das SR, Deo R, de Ferranti SD, Floyd J, Fornage M, Gillespie C *et al* (2017) Heart disease and stroke statistics-2017 update: a report from the American Heart Association. *Circulation* 135: e146–e603
- Beyaz S, Kim JH, Pinello L, Xifaras ME, Hu Y, Huang J, Kerenyi MA, Das PP, Barnitz RA, Heralut A *et al* (2017) The histone demethylase UTX regulates the lineage-specific epigenetic program of invariant natural killer T cells. *Nat Immunol* 18: 184–195
- Brown JD, Lin CY, Duan Q, Griffin G, Federation A, Paranal RM, Bair S, Newton G, Lichtman A, Kung A *et al* (2014a) Gene Expression Omnibus GSE53998 (<https://www.ncbi.nlm.nih.gov/geo/query/acc.cgi?acc=GSE53998>) [DATASET]
- Brown JD, Lin CY, Duan Q, Griffin G, Federation A, Paranal RM, Bair S, Newton G, Lichtman A, Kung A *et al* (2014b) NF-kappaB directs dynamic super enhancer formation in inflammation and atherogenesis. *Mol Cell* 56: 219–231
- Cancer Genome Atlas Research N, Ley TJ, Miller C, Ding L, Raphael BJ, Mungall AJ, Robertson A, Hoadley K, Triche TJ Jr, Laird PW *et al* (2013) Genomic and epigenomic landscapes of adult de novo acute myeloid leukemia. *N Engl J Med* 368: 2059–2074
- Chen JY, Li CF, Chu PY, Lai YS, Chen CH, Jiang SS, Hou MF, Hung WC (2016) Lysine demethylase 2A promotes stemness and angiogenesis of breast cancer by upregulating Jagged1. *Oncotarget* 7: 27689–27710
- Dalgliesh GL, Furge K, Greenman C, Chen L, Bignell G, Butler A, Davies H, Edkins S, Hardy C, Latimer C *et al* (2010) Systematic sequencing of renal carcinoma reveals inactivation of histone modifying genes. *Nature* 463: 360–363
- De Santa F, Totaro MG, Prosperini E, Notarbartolo S, Testa G, Natoli G (2007) The histone H3 lysine-27 demethylase Jmjd3 links inflammation to inhibition of polycomb-mediated gene silencing. *Cell* 130: 1083–1094
- De Santa F, Narang V, Yap ZH, Tusi BK, Burgold T, Austenaa L, Bucci G, Caganova M, Notarbartolo S, Casola S *et al* (2009) Jmjd3 contributes to the control of gene expression in LPS-activated macrophages. *EMBO J* 28: 3341–3352
- Dixon JR, Selvaraj S, Yue F, Kim A, Li Y, Shen Y, Hu M, Liu JS, Ren B (2012) Topological domains in mammalian genomes identified by analysis of chromatin interactions. *Nature* 485: 376–380
- Dixon JR, Jung I, Selvaraj S, Shen Y, Antosiewicz-Bourget JE, Lee AY, Ye Z, Kim A, Rajagopal N, Xie W *et al* (2015) Chromatin architecture reorganization during stem cell differentiation. *Nature* 518: 331–336
- Dowen JM, Fan ZP, Hnisz D, Ren G, Abraham BJ, Zhang LN, Weintraub AS, Schujiers J, Lee TI, Zhao K *et al* (2014) Control of cell identity genes occurs in insulated neighborhoods in mammalian chromosomes. *Cell* 159: 374–387
- Fang TC, Schaefer U, Mecklenbrauker I, Stienen A, Dewell S, Chen MS, Rioja I, Parravicini V, Prinjha RK, Chandwani R *et al* (2012) Histone H3 lysine 9 dimethylation as an epigenetic signature of the interferon response. *J Exp Med* 209: 661–669
- FANTOM Consortium and the RIKEN PMI and CLST, Forrest AR, Kawaji H, Rehli M, Baillie JK, de Hoon MJ, Haberle V, Lassmann T, Kulakovskiy IV, Lizio M *et al* (2014) A promoter-level mammalian expression atlas. *Nature* 507: 462–470
- Faralli H, Wang C, Nakka K, Benyoucef A, Sebastian S, Zhuang L, Chu A, Palii CG, Liu C, Camellato B *et al* (2016) UTX demethylase activity is required for satellite cell-mediated muscle regeneration. *J Clin Invest* 126: 1555–1565
- Feinberg MW, Moore KJ (2016) MicroRNA regulation of atherosclerosis. *Circ Res* 118: 703–720
- Fullwood MJ, Liu MH, Pan YF, Liu J, Xu H, Mohamed YB, Orlov YL, Velkov S, Ho A, Mei PH *et al* (2009) An oestrogen-receptor-alpha-bound human chromatin interactome. *Nature* 462: 58–64
- Garcia DM, Baek D, Shin C, Bell GW, Grimson A, Bartel DP (2011) Weak seed-pairing stability and high target-site abundance decrease the proficiency of Isy-6 and other microRNAs. *Nat Struct Mol Biol* 18: 1139–1146
- Ghosh GC, Bhadra R, Ghosh RK, Banerjee K, Gupta A (2017) RVX208: a novel BET protein inhibitor, role as an inducer of apo A-I/HDL and beyond. *Cardiovasc Ther* 35: e12265
- Gistera A, Hansson GK (2017) The immunology of atherosclerosis. *Nat Rev Nephrol* 13: 368–380
- Gui Y, Guo G, Huang Y, Hu X, Tang A, Gao S, Wu R, Chen C, Li X, Zhou L *et al* (2011) Frequent mutations of chromatin remodeling genes in transitional cell carcinoma of the bladder. *Nat Genet* 43: 875–878
- van Haften G, Dalgliesh GL, Davies H, Chen L, Bignell G, Greenman C, Edkins S, Hardy C, O'Meara S, Teague J *et al* (2009) Somatic mutations of the histone H3K27 demethylase gene UTX in human cancer. *Nat Genet* 41: 521–523
- Hah N, Benner C, Chong LW, Yu RT, Downes M, Evans RM (2015) Inflammation-sensitive super enhancers form domains of coordinately regulated enhancer RNAs. *Proc Natl Acad Sci USA* 112: E297–E302
- Handoko L, Xu H, Li G, Ngan CY, Chew E, Schnapp M, Lee CW, Ye C, Ping JL, Mulawadi F *et al* (2011) CTCF-mediated functional chromatin interactome in pluripotent cells. *Nat Genet* 43: 630–638
- Hashizume R, Andor N, Ihara Y, Lerner R, Gan H, Chen X, Fang D, Huang X, Tom MW, Ngo V *et al* (2014) Pharmacologic inhibition of histone demethylation as a therapy for pediatric brainstem glioma. *Nat Med* 20: 1394–1396
- Heinz S, Romanoski CE, Benner C, Glass CK (2015) The selection and function of cell type-specific enhancers. *Nat Rev Mol Cell Biol* 16: 144–154

- Hnisz D, Abraham BJ, Lee TI, Lau A, Saint-Andre V, Sigova AA, Hoke HA, Young RA (2013) Super-enhancers in the control of cell identity and disease. *Cell* 155: 934–947
- Hnisz D, Weintraub AS, Day DS, Valton AL, Bak RO, Li CH, Goldmann J, Lajoie BR, Fan ZP, Sigova AA et al (2016) Activation of proto-oncogenes by disruption of chromosome neighborhoods. *Science* 351: 1454–1458
- Hnisz D, Shrinivas K, Young RA, Chakraborty AK, Sharp PA (2017) A phase separation model for transcriptional control. *Cell* 169: 13–23
- Hogan NT, Whalen MB, Stolze LK, Hadeli NK, Lam MT, Springstead JR, Glass CK, Romanoski CE (2017) Transcriptional networks specifying homeostatic and inflammatory programs of gene expression in human aortic endothelial cells. *Elife* 6: e22536
- Horton JR, Upadhyay AK, Qi HH, Zhang X, Shi Y, Cheng X (2010) Enzymatic and structural insights for substrate specificity of a family of jumonji histone lysine demethylases. *Nat Struct Mol Biol* 17: 38–43
- Huether R, Dong L, Chen X, Wu G, Parker M, Wei L, Ma J, Edmonson MN, Hedlund EK, Rusch MC et al (2014) The landscape of somatic mutations in epigenetic regulators across 1,000 paediatric cancer genomes. *Nat Commun* 5: 3630
- Inoue K, Kobayashi M, Yano K, Miura M, Izumi A, Mataka C, Doi T, Hamakubo T, Reid PC, Hume DA et al (2006) Histone deacetylase inhibitor reduces monocyte adhesion to endothelium through the suppression of vascular cell adhesion molecule-1 expression. *Arterioscler Thromb Vasc Biol* 26: 2652–2659
- Inoue T, Kohro T, Tanaka T, Kanki Y, Li G, Poh HM, Mimura I, Kobayashi M, Taguchi A, Maejima T et al (2014) Cross-enhancement of ANGPTL4 transcription by HIF1 alpha and PPAR beta/delta is the result of the conformational proximity of two response elements. *Genome Biol* 15: R63
- Ito S, Osaka M, Edamatsu T, Itoh Y, Yoshida M (2016) Crucial role of the aryl hydrocarbon receptor (AhR) in indoxyl sulfate-induced vascular inflammation. *J Atheroscler Thromb* 23: 960–975
- Jin F, Li Y, Dixon JR, Selvaraj S, Ye Z, Lee AY, Yen CA, Schmitt AD, Espinoza CA, Ren B (2013) A high-resolution map of the three-dimensional chromatin interactome in human cells. *Nature* 503: 290–294
- Kanki Y, Kohro T, Jiang S, Tsutsumi S, Mimura I, Suehiro J, Wada Y, Ohta Y, Ihara S, Iwanari H et al (2011) Epigenetically coordinated GATA2 binding is necessary for endothelium-specific endomucin expression. *EMBO J* 30: 2582–2595
- Kanki Y, Nakaki R, Shimamura T, Matsunaga T, Yamamizu K, Katayama S, Suehiro J, Osawa T, Aburatani H, Kodama T et al (2017) Dynamically and epigenetically coordinated GATA/ETS/SOX transcription factor expression is indispensable for endothelial cell differentiation. *Nucleic Acids Res* 45: 4344–4358
- Kim D, Perteau G, Trapnell C, Pimentel H, Kelley R, Salzberg SL (2013) TopHat2: accurate alignment of transcriptomes in the presence of insertions, deletions and gene fusions. *Genome Biol* 14: R36
- Kim YH, Marhon SA, Zhang Y, Steger DJ, Won KJ, Lazar MA (2018) Rev-erbalpha dynamically modulates chromatin looping to control circadian gene transcription. *Science* 359: 1274–1277
- Kruidenier L, Chung CW, Cheng Z, Liddle J, Che K, Joberty G, Bantscheff M, Bountra C, Bridges A, Diallo H et al (2012) A selective jumonji H3K27 demethylase inhibitor modulates the proinflammatory macrophage response. *Nature* 488: 404–408
- Kruse K, Hug CB, Hernandez-Rodriguez B, Vaquerizas JM (2016) TADtool: visual parameter identification for TAD-calling algorithms. *Bioinformatics* 32: 3190–3192
- Kurimoto K, Yabuta Y, Hayashi K, Ohta H, Kiyonari H, Mitani T, Moritoki Y, Kohri K, Kimura H, Yamamoto T et al (2015) Quantitative dynamics of chromatin remodeling during germ cell specification from mouse embryonic stem cells. *Cell Stem Cell* 16: 517–532
- Lan F, Bayliss PE, Rinn JL, Whetstone JR, Wang JK, Chen S, Iwase S, Alpatov R, Issaeva I, Canaani E et al (2007) A histone H3 lysine 27 demethylase regulates animal posterior development. *Nature* 449: 689–694
- Lee MG, Villa R, Trojer P, Norman J, Yan KP, Reinberg D, Di Croce L, Shiekhhattar R (2007) Demethylation of H3K27 regulates polycomb recruitment and H2A ubiquitination. *Science* 318: 447–450
- Lee S, Lee JW, Lee SK (2012) UTX, a histone H3-lysine 27 demethylase, acts as a critical switch to activate the cardiac developmental program. *Dev Cell* 22: 25–37
- Li G, Fullwood MJ, Xu H, Mulawadi FH, Velkov S, Vega V, Ariyaratne PN, Mohamed YB, Ooi HS, Tennakoon C et al (2010) ChIA-PET tool for comprehensive chromatin interaction analysis with paired-end tag sequencing. *Genome Biol* 11: R22
- Libby P (2002) Inflammation in atherosclerosis. *Nature* 420: 868–874
- Libby P, Ridker PM, Hansson GK (2011) Progress and challenges in translating the biology of atherosclerosis. *Nature* 473: 317–325
- Lieberman-Aiden E, van Berkum NL, Williams L, Imakaev M, Ragozy T, Telling A, Amit I, Lajoie BR, Sabo PJ, Dorschner MO et al (2009) Comprehensive mapping of long-range interactions reveals folding principles of the human genome. *Science* 326: 289–293
- Loven J, Hoke HA, Lin CY, Lau A, Orlando DA, Vakoc CR, Bradner JE, Lee TI, Young RA (2013) Selective inhibition of tumor oncogenes by disruption of super-enhancers. *Cell* 153: 320–334
- Mahony S, Benos PV (2007) STAMP: a web tool for exploring DNA-binding motif similarities. *Nucleic Acids Res* 35: W253–W258
- Matys V, Fricke E, Geffers R, Gossling E, Haubrock M, Hehl R, Hornischer K, Karas D, Kel AE, Kel-Margoulis OV et al (2003) TRANSFAC: transcriptional regulation, from patterns to profiles. *Nucleic Acids Res* 31: 374–378
- McLean CY, Bristol D, Hiller M, Clarke SL, Schaar BT, Lowe CB, Wenger AM, Bejerano G (2010) GREAT improves functional interpretation of cis-regulatory regions. *Nat Biotechnol* 28: 495–501
- Mimura I, Nangaku M, Kanki Y, Tsutsumi S, Inoue T, Kohro T, Yamamoto S, Fujita T, Shimamura T, Suehiro J et al (2012) Dynamic change of chromatin conformation in response to hypoxia enhances the expression of GLUT3 (SLC2A3) by cooperative interaction of hypoxia-inducible factor 1 and KDM3A. *Mol Cell Biol* 32: 3018–3032
- Mozzetta C, Pontis J, Fritsch L, Robin P, Portoso M, Proux C, Margueron R, Ait-Si-Ali S (2014) The histone H3 lysine 9 methyltransferases G9a and GLP regulate polycomb repressive complex 2-mediated gene silencing. *Mol Cell* 53: 277–289
- Mumbach MR, Rubin AJ, Flynn RA, Dai C, Khavari PA, Greenleaf WJ, Chang HY (2016) HiChIP: efficient and sensitive analysis of protein-directed genome architecture. *Nat Methods* 13: 919–922
- Nakaki R, Kang J, Tateno M (2012) A novel ab initio identification system of transcriptional regulation motifs in genome DNA sequences based on direct comparison scheme of signal/noise distributions. *Nucleic Acids Res* 40: 8835–8848
- Ntziachristos P, Tsirigos A, Welstead GG, Trimarchi T, Bakogianni S, Xu L, Loizou E, Holmfeldt L, Strikoudis A, King B et al (2014) Contrasting roles of histone 3 lysine 27 demethylases in acute lymphoblastic leukaemia. *Nature* 514: 513–517
- Ogiyama Y, Schuettengruber B, Papadopoulos GL, Chang JM, Cavalli G (2018) Polycomb-dependent chromatin looping contributes to gene silencing during *Drosophila* development. *Mol Cell* 71: 73–88 e5
- Osaka M, Hagita S, Haraguchi M, Kajimura M, Suematsu M, Yoshida M (2007) Real-time imaging of mechanically injured femoral artery in mice reveals a biphasic pattern of leukocyte accumulation. *Am J Physiol Heart Circ Physiol* 292: H1876–H1882

- Osawa T, Muramatsu M, Wang F, Tsuchida R, Kodama T, Minami T, Shibuya M (2011) Increased expression of histone demethylase JHDM1D under nutrient starvation suppresses tumor growth via down-regulating angiogenesis. *Proc Natl Acad Sci USA* 108: 20725–20729
- Papantonis A, Kohro T, Baboo S, Larkin JD, Deng B, Short P, Tsutsumi S, Taylor S, Kanki Y, Kobayashi M et al (2012) TNF α signals through specialized factories where responsive coding and miRNA genes are transcribed. *EMBO J* 31: 4404–4414
- Parker SC, Stitzel ML, Taylor DL, Orozco JM, Erdos MR, Akiyama JA, van Bueren KL, Chines PS, Narisu N, Program NCS et al (2013) Chromatin stretch enhancer states drive cell-specific gene regulation and harbor human disease risk variants. *Proc Natl Acad Sci USA* 110: 17921–17926
- Phillips-Cremins JE, Sauria ME, Sanyal A, Gerasimova TI, Lajoie BR, Bell JS, Ong CT, Hookway TA, Guo C, Sun Y et al (2013) Architectural protein subclasses shape 3D organization of genomes during lineage commitment. *Cell* 153: 1281–1295
- Pott S, Lieb JD (2015) What are super-enhancers? *Nat Genet* 47: 8–12
- Rao SS, Huntley MH, Durand NC, Stamenova EK, Bochkov ID, Robinson JT, Sanborn AL, Machol I, Omer AD, Lander ES et al (2014) A 3D map of the human genome at kilobase resolution reveals principles of chromatin looping. *Cell* 159: 1665–1680
- de Rie D, Abugessaisa I, Alam T, Arner E, Arner P, Ashoor H, Astrom G, Babina M, Bertin N, Burroughs AM et al (2017) An integrated expression atlas of miRNAs and their promoters in human and mouse. *Nat Biotechnol* 35: 872–878
- Roadmap Epigenomics C, Kundaje A, Meuleman W, Ernst J, Bilenyk M, Yen A, Heravi-Moussavi A, Kheradpour P, Zhang Z, Wang J et al (2015) Integrative analysis of 111 reference human epigenomes. *Nature* 518: 317–330
- Saccani S, Natoli G (2002) Dynamic changes in histone H3 Lys 9 methylation occurring at tightly regulated inducible inflammatory genes. *Genes Dev* 16: 2219–2224
- Saint-Andre V, Federation AJ, Lin CY, Abraham BJ, Reddy J, Lee TI, Bradner JE, Young RA (2016) Models of human core transcriptional regulatory circuitries. *Genome Res* 26: 385–396
- Schmidt SF, Larsen BD, Loft A, Nielsen R, Madsen JG, Mandrup S (2015) Acute TNF-induced repression of cell identity genes is mediated by NF κ B-directed redistribution of cofactors from super-enhancers. *Genome Res* 25: 1281–1294
- Seenundun S, Rampalli S, Liu QC, Aziz A, Palii C, Hong S, Blais A, Brand M, Ge K, Dilworth FJ (2010) UTX mediates demethylation of H3K27me3 at muscle-specific genes during myogenesis. *EMBO J* 29: 1401–1411
- Servant N, Varoquaux N, Lajoie BR, Viara E, Chen CJ, Vert JP, Heard E, Dekker J, Barillot E (2015) HiC-Pro: an optimized and flexible pipeline for Hi-C data processing. *Genome Biol* 16: 259
- Shen L, Shao N, Liu X, Nestler E (2014) ngs.plot: quick mining and visualization of next-generation sequencing data by integrating genomic databases. *BMC Genom* 15: 284
- Siersbaek R, Madsen JGS, Javierre BM, Nielsen R, Bagge EK, Cairns J, Wingett SW, Traynor S, Spivakov M, Fraser P et al (2017) Dynamic rewiring of promoter-anchored chromatin loops during adipocyte differentiation. *Mol Cell* 66: 420–435 e5
- Suarez Y, Wang C, Manes TD, Pober JS (2010) Cutting edge: TNF-induced microRNAs regulate TNF-induced expression of E-selectin and intercellular adhesion molecule-1 on human endothelial cells: feedback control of inflammation. *J Immunol* 184: 21–25
- Suzuki HI, Young RA, Sharp PA (2017) Super-enhancer-mediated RNA processing revealed by integrative MicroRNA network analysis. *Cell* 168: 1000–1014 e15
- Tang Z, Luo OJ, Li X, Zheng M, Zhu JJ, Szalaj P, Trzaskoma P, Magalska A, Wlodarczyk J, Rusczycki B et al (2015) CTCF-mediated human 3D genome architecture reveals chromatin topology for transcription. *Cell* 163: 1611–1627
- Tozawa H, Kanki Y, Suehiro J, Tsutsumi S, Kohro T, Wada Y, Aburatani H, Aird WC, Kodama T, Minami T (2011) Genome-wide approaches reveal functional interleukin-4-inducible STAT6 binding to the vascular cell adhesion molecule 1 promoter. *Mol Cell Biol* 31: 2196–2209
- Trapnell C, Williams BA, Pertea G, Mortazavi A, Kwan G, van Baren MJ, Salzberg SL, Wold BJ, Pachter L (2010) Transcript assembly and quantification by RNA-Seq reveals unannotated transcripts and isoform switching during cell differentiation. *Nat Biotechnol* 28: 511–515
- Tsukada Y, Ishitani T, Nakayama KI (2010) KDM7 is a dual demethylase for histone H3 Lys 9 and Lys 27 and functions in brain development. *Genes Dev* 24: 432–437
- Wang SP, Tang Z, Chen CW, Shimada M, Koche RP, Wang LH, Nakadai T, Chramiec A, Krivtsov AV, Armstrong SA et al (2017) A UTX-MLL4-p300 transcriptional regulatory network coordinately shapes active enhancer landscapes for eliciting transcription. *Mol Cell* 67: 308–321 e6
- Whyte WA, Orlando DA, Hnisz D, Abraham BJ, Lin CY, Kagey MH, Rahl PB, Lee TI, Young RA (2013) Master transcription factors and mediator establish super-enhancers at key cell identity genes. *Cell* 153: 307–319
- Zhang Y, Liu T, Meyer CA, Eickhout J, Johnson DS, Bernstein BE, Nusbaum C, Myers RM, Brown M, Li W et al (2008) Model-based analysis of ChIP-Seq (MACS). *Genome Biol* 9: R137
- Zhang Q, Lenardo MJ, Baltimore D (2017) 30 years of NF- κ B: a blossoming of relevance to human pathobiology. *Cell* 168: 37–57
- Zylicz JJ, Dietmann S, Gunesdogan U, Hackett JA, Cougot D, Lee C, Surani MA (2015) Chromatin dynamics and the role of G9a in gene regulation and enhancer silencing during early mouse development. *Elife* 4: e09571